Geobiology

Geobiology (2012), **10**, 402–423 DOI: 10.1111/j.1472-4669.2012.00332.x

Thermally-induced structural and chemical alteration of organic-walled microfossils: an experimental approach to understanding fossil preservation in metasediments

J. D. SCHIFFBAUER,[1,2,3] A. F. WALLACE,[4] J. L. HUNTER JR,[2] M. KOWALEWSKI,[5] R. J. BODNAR[3] AND S. XIAO[3]

[1]*Department of Geological Sciences, University of Missouri, Columbia, MO, USA*
[2]*Nanoscale Characterization and Fabrication Laboratory, Institute for Critical Technology and Applied Science, Virginia Polytechnic Institute and State University, Blacksburg, VA, USA*
[3]*Department of Geosciences, Virginia Polytechnic Institute and State University, Blacksburg, VA, USA*
[4]*Earth Sciences Division, Lawrence Berkeley National Laboratory, University of California, Berkeley, Berkeley, CA, USA*
[5]*Florida Museum of Natural History, University of Florida, Gainesville, FL, USA*

ABSTRACT

The identification and confirmation of *bona fide* Archean–Paleoproterozoic microfossils can prove to be a challenging task, further compounded by diagenetic and metamorphic histories. While structures of likely biological origin are not uncommon in Precambrian rocks, the search for early fossil life has been disproportionately focused on lesser thermally altered rocks, typically greenschist or lower-grade metamorphism. Recently, however, an increasing number of inferred micro- and macrofossils have been reported from higher-grade metasediments, prompting us to experimentally test and quantify the preservability of organic-walled microfossils over varying durations of controlled heating and under two differing redox conditions. Because of their relatively low-intensity natural thermal alteration, acritarchs from the Mesoproterozoic Ruyang Group were chosen as subjects for experimental heating at approximately 500°C, with durations ranging from 1 to 250 days and in both oxic (normal present day conditions) and anoxic conditions. Upon extraction, the opacity, reflectivity, color, microchemistry, and microstructures of the heated acritarchs were characterized using optic microscopy, scanning electron microscopy, Raman spectroscopy, and X-ray photoelectron spectroscopy. The results differ for acritarchs prepared under oxic vs. anoxic conditions, with the anoxic replicates surviving experimental heating longer and retaining biological morphologies better, despite an increasing degree of carbonization with continuous heating. Conversely, the oxic replicates show aggressive degradation. In conjunction with fossils from high-grade metasediments, our data illustrate the preservational potential of organic-walled microfossils subjected to metamorphism in reducing conditions, offer insights into the search for microfossils in metasediments, and help to elucidate the influence of time on the carbonization/graphitization processes during thermal alteration.

Received 19 September 2011; accepted 02 April 2012

Corresponding author: J. D. Schiffbauer. Tel.: 1 540 557 7356; fax: 1 540 231 3386; e-mail: jdschiff@vt.edu

INTRODUCTION

The deeper into geologic time we travel in the search for evidence of life, the more challenging the investigation becomes. First and foremost, prior to the Neoproterozoic, life was dominated by single-cell forms, most of which were microscopic, morphologically unsophisticated, and exceedingly difficult to recognize through field observations. Pre-Neoproterozoic paleobiological investigation, therefore, is by necessity a twofold process involving (i) identification of potential biological forms and (ii) verification of biogenicity. The latter task can be challenging, especially when dealing with fossils displaying simple morphologies that have experienced millions to billions of years of diagenetic and metamorphic alteration.

The investigation of microscopic life on Earth today has provided Precambrian paleobiologists with relative morphological and biochemical standards of biogenicity for single-celled fossils. For example, modern prokaryotes occupy four basic morphologies—cocci (spheres), bacilli (rods), spirilli

(spirals), and vibrio (commas or kidney beans)—and, for the vast majority, reside in a fairly narrow size range between 2 and 10 μm. In addition to relative size and shape, cellular constituents and metabolic functions of modern prokaryotic life have been very well studied and classified. Following these modern morphological and biochemical characterizations, paleobiologists have an existing guide when they investigate Archean–Mesoproterozoic rocks for morphological regularities and/or molecular biosignatures, including complex organic hydrocarbon or cellular-constituent biomarkers (Summons *et al.*, 1999) and various isotopic shifts in minerals reflecting ancient microbial metabolic processes (Ohmoto *et al.*, 1993; Horita, 2005; Papineau & Mojzsis, 2006).

However, morphological and biochemical characteristics used for the identification of unicellular life on Earth today are altered not only during the initial taphonomic processes responsible for their fossilization, but also during later diagenetic and metamorphic processes affecting the host rock. As such, the general paleobiological perception is that metamorphic heating and deformation are detrimental to the preservation of life's signals. Unfortunately, for paleobiologists interested in early evolution, much of the available Archean–Paleoproterozoic rocks have experienced extensive metamorphism. Under these harsh conditions, biological features, such as color or morphology, are commonly expected to be altered, sometimes beyond recognition (e.g., Brasier *et al.*, 2002). For instance, organic-walled microfossils, typically yellowish to brownish-orange in color when preserved in non-metamorphosed rocks, are darkened toward black during metamorphism (the gradient of this color change is fundamental to Batten's thermal alteration index; Batten, 1996). Not only can morphological or biochemical signatures of life be distorted or even destroyed entirely by metamorphic processes, these same processes can generate abiotic but biologically mimicking doppelgängers. These abiotic imposters undoubtedly can lead (and have led) to misidentification and misinterpretation of the fossil record of early life (Hofmann & Schopf, 1983; Schopf & Walter, 1983; Mendelson & Schopf, 1992). Further, metamorphic processes have the capability of transforming complex organic hydrocarbons and disordered carbonaceous materials into ordered graphitic materials (Buseck & Huang, 1985; Wopenka & Pasteris, 1993; Beyssac *et al.*, 2002b)—albeit intrinsically difficult for some types of organic matter to graphitize, such as carbonaceous material exhibiting high microporosity and/or low oxygen fugacity (Bény-Bassez & Rouzaud, 1985; Large *et al.*, 1994). To make things even more complicated, graphite generated from biological precursors can be microchemically indistinguishable from well-ordered abiotic graphite-derived *de novo* from metamorphism, both in terms of carbon isotopic composition (Van Zuilen *et al.*, 2002) and Raman characterization (Pasteris & Wopenka, 2002), and thus, a combination of independent but mutually reinforcing morphological and biogeochemical data should be used to verify biogenicity (Schopf *et al.*, 2002). Thus, the summation of taphonomic and diagenetic modifications to microfossil morphology and biochemistry—or 'Archeanization' (termed as such by Knoll *et al.*, 1988)—presents serious challenges to early life exploration and raises the question: can we institute a means for distinguishing veritable biological remains (even when they are metamorphically modified) from abiotically generated imposters?

Implications of ancient graphitized microfossils from high-grade metamorphic rocks

Numerous Archean–Paleoproterozoic microfossils with recognizable biological morphologies have been reported, an abundance of which are hosted in lower-grade metacherts (Knoll & Barghoorn, 1977; Awramik *et al.*, 1983; Schopf & Walter, 1983; Walsh & Lowe, 1985; Altermann & Schopf, 1995; Schopf, 2006). It is widely known that organic-walled microfossils can survive greenschist-grade metamorphism (Kidder & Awramik, 1990; Knoll, 1992; Butterfield, 1995; Molyneux, 1998; Orr *et al.*, 1998; Powell, 2003; Butterfield *et al.*, 2007), but rocks metamorphosed beyond greenschist-grade have been underrepresented in paleontological exploration. However, recent studies of higher-grade Precambrian and Phanerozoic rocks have shown that *bona fide* filamentous bacteria, acritarchs (including both leiospheres and potential acanthomorphs), lycophyte megaspores, chitinozoans, possible paraconodonts, and pteridophyll leaf fragments can be preserved in greenschist-amphibolite-grade metasediments and metachert lenses (Squire *et al.*, 2006; Zang, 2007), amphibolite-grade carbonaceous quartzites (Schiffbauer *et al.*, 2007) and graphitic schists (Franz *et al.*, 1991), blueschist grade carbonates (Bernard *et al.*, 2007), and gneisses (Hanel *et al.*, 1999). Specifically important to the experimental approach reported here, two of the above-mentioned studies reported partially to completely graphitized acritarchs—some with acanthomorphic morphologies and others with distinct marginal folds, fine surficial wrinkles, nm-scale pores, and two discrete vesicle walls—from high-grade metachert lenses and carbonaceous quartzites (Schiffbauer *et al.*, 2007; Zang, 2007). In conjunction with detailed characterization of natural representatives, analysis of the experimentally heated microfossils herein provides both understanding of the taphonomic processes that contribute to the preservation and alteration of fossils in high-grade metasediments and new insights into the paleontological search for ancient life within metamorphic rocks.

Observing the processes of carbonization and graphitization

The transformation of carbonaceous material into graphite has been studied in both natural and experimental settings by diverse analytical means, including optical microscopy,

scanning and transmission electron microscopy, focused ion beam electron microscopy, X-ray diffraction, Raman spectroscopy, and stable isotope analyses (e.g., Bény-Bassez & Rouzaud, 1985; Buseck & Huang, 1985; Pasteris & Wopenka, 1991; Wopenka & Pasteris, 1993; Beyssac *et al.*, 2002a,b; Schopf *et al.*, 2005; Bernard *et al.*, 2007). In general, thermal treatment of carbonaceous materials results in volatilization of H-, O-, and N-bearing functional groups to yield a nearly pure and relatively amorphous carbon phase. In metamorphic settings, this *carbonization* process produces disordered precursor material that, with extended exposure to elevated temperature/pressure conditions, transforms to crystalline graphite alongside concomitant changes in porosity through a process known as *graphitization*. While graphitization is typically assumed to occur above 900 °C (and carbonization from approximately 500 to 900 °C; see Fitzer *et al.*, 1971; Fischbach, 1971; Schopf *et al.*, 2005), the specific influences of metamorphic temperatures and pressures on the crystallization of carbonaceous materials in nature are debated because of dependence on various other factors (e.g., duration of metamorphism, composition of initial carbonaceous material). The commonly held view is that the disorder to order transition in natural settings is predominantly controlled by temperature, and secondarily influenced by pressure and duration of metamorphism (e.g., Landis, 1971; Wopenka & Pasteris, 1993; Wada *et al.*, 1994), a view that has been supported by experimental analyses (Beyssac *et al.*, 2003). This essentially may be thought of as an annealing process, in which prolonged exposure to heat (and secondarily pressure) enables large energy barriers opposing reorganization of the disordered carbon matrix to be overcome resulting in the emergence of ordered regions with relatively low defect densities. While the ordering of carbon in metamorphically produced graphite does not correlate with the degree of metamorphic pressure experienced, it has been demonstrated in experimental studies that pressure plays an integral role in inducing microstructural alterations (Beyssac *et al.*, 2003), perhaps by influencing the kinetics of the crystallization processes. These changes, most importantly the structural modification of microporous precursors to lamellar microtextures, are necessary components of the graphitization of microtexturally heterogeneous carbonaceous materials, such as those that are biologically derived (Beyssac *et al.*, 2002b, 2003). As temperature is the principal factor in graphitization, the progressive stages of metamorphically influenced graphitization can be used as a proxy for the peak metamorphic temperature experienced by the carbonaceous materials (e.g., Pasteris & Wopenka, 1991; Jehlička & Bény, 1992; Wopenka & Pasteris, 1993; Beyssac *et al.*, 2002a, 2004). The influence of time on the graphitization process remains largely understudied from experimental protocols with short heating durations (i.e., Beyssac *et al.*, 2003; Schopf *et al.*, 2005). If time plays a role in the progression of the carbonization/graphitization processes, one may anticipate that lengthened periods of heating would likely result in increasingly ordered carbonaceous materials until all available carbon resides in the crystalline graphite lattice (or at least an intermediate metastable state; Beyssac *et al.*, 2003).

Sedimentary rocks generally contain varying amounts of carbonaceous material that starts out being poorly ordered organic matter derived from metabolic processes (e.g., proteins, lipids, and carbohydrates). When this material is subjected to metamorphism, it eventually evolves into well-ordered graphite and may record isotopic signals of biological activity (Mojzsis *et al.*, 1996). In addition to isotopic signatures, studies have indicated that ancient micro-organisms themselves can in fact be preserved in higher-grade metasediments (Hanel *et al.*, 1999; Squire *et al.*, 2006; Bernard *et al.*, 2007; Schiffbauer *et al.*, 2007; Zang, 2007); however, the conditions under which this preservation occurs, the microthermochemical transformation which these fossils undergo, and the taphonomic potential for retention of recognizable microfossil morphologies has not been extensively tested.

Following similar experimentation by Schopf *et al.* (2005) as well as experimental conodont heating by Marshall *et al.* (2001), the study presented here utilizes an experimental approach in an attempt to bolster our understanding of the taphonomic processes that affect the preservation of organic-walled microfossils exposed to higher-grade metamorphic temperatures. In contrast to the study by Schopf *et al.* (2005), which varied heating temperatures over 2 h periods, our approach maintained a constant temperature of 500 ± 2.5 °C (at 1 atm pressure) and varied the heating times, from 24 h to 250 days. In an effort to maximize the observable effects of temperature over time, the temperature threshold of 500 °C was selected for two primary reasons. First, from the Schopf *et al.* (2005) study, it was suggested that an enlargement of polyaromatic hydrocarbons and an accompanying loss of peripheral hydrogens likely began at the temperature window between 500 and 900 °C, a result in agreement with modeling studies of graphitization (Negri *et al.*, 2002). Second, natural representatives, in the form of graphitized acritarchs with recognizable biological morphologies, have been recovered from rocks experiencing a peak metamorphic temperature of just over approximately 500 °C (Schiffbauer *et al.*, 2007). To test the effect of redox conditions, the heating experiments were carried out in both oxic and anoxic media. Both heated and unheated (control) acritarch specimens were analyzed using a diverse array of methods to characterize the influence of time and oxygen availability on carbonization/graphitization and morphologies of the heated organic-walled microfossils. The techniques applied here included optical microscopy, ordinal and presence–absence thermal alteration scoring systems, color intensity analysis of digital photomicrographs, Raman spectroscopy, X-ray photoelectron spectroscopy (XPS), and scanning electron microscopy (SEM).

EXPERIMENTAL METHODS

Acritarch sample description

The fossiliferous shale sample (SYG 6) used for this study was collected from the non-metamorphosed to weakly metamorphosed Beidajian Formation, Ruyang Group, at the Shuiyougou Section in southern Shanxi, China (Xiao *et al.*, 1997). The age of the Ruyang Group is bracketed between 1625 and 1000 Ma, and C-isotopic chemostratigraphic data suggest an age of 1400–1300 Ma (Xiao *et al.*, 1997). Carbonaceous shale and siltstone of the Beidajian Formation at the Shuiyougou Section contain highly abundant and well-preserved acritarchs, including *Valeria lophostriata*, *Spiromorpha segmentata*, *Tappania plana*, *Shuiyousphaeridium macroreticulatum*, and *Dictyosphaera delicata* (Yin, 1997; Yin *et al.*, 2005), of which *T. plana* has been reported from Mesoproterpzoic rocks in Australia, Siberia, and India (Javaux *et al.*, 2001; Prasad & Asher, 2001; Prasad *et al.*, 2005; Nagovitsin, 2009). *D. delicata* and *S. macroreticulatum* are the most abundant among these taxa. Their vesicle walls consist of an interlocking polygonal plate construction. *D. delicata* is herkomorphic and lacks extravesicular processes, whereas *S. macroreticulatum* is acanthomorphic with unevenly distributed processes on the exterior vesicle surface. Because of their similar vesicular structure, it has been suggested that these two acritarch species may actually be conspecific, with the smaller *D. delicata* potentially representing an earlier developmental stage of the larger *S. macroreticulatum* (Xiao *et al.*, 1997). Alternatively, it is possible that the smaller *D. delicata* vesicles may have lost their (likely less robust) processes during diagenesis or sample preparation/extraction (Xiao *et al.*, 1997). The polygonal reticulations from both species are approximately 1.5–3 μm in maximum width and are defined by raised ridges on the outer vesicle surface (and corresponding polygonal cracks on the inner surface) that are approximately 100–300 nm thick and 100–200 nm high (Xiao *et al.*, 1997; Javaux *et al.*, 2004; Schiffbauer & Xiao, 2009).

Heating and preparation

Shale chips selected for this study were first examined using reflected light optical microscopy to verify the presence of acritarchs. A 1.2 g sample of unheated shale was macerated via standard palynological hydrofluoric acid digestion (Vidal, 1988) to establish both a set of baseline acritarchs (10 individuals to serve as a yardstick for thermal alteration scoring, see section 'Optical microscopy, thermal alteration scoring, and digital photomicrograph analysis') and a group of control acritarchs (50 individuals to be compared with heated acritarchs). In the heating experiment, shale chips were lightly crushed to ≥500 μm-size fragments and placed in gold capsules. For initial preparation of the capsules, gold tubes (0.5 cm outer diameter) were cut into 3.0–4.0 cm sections (initial empty capsule weight 3.4–4.8 g) and cold-welded at one end. Subsequently, two separate loading methods were utilized for oxic and anoxic heating. For oxic heating, 0.50–0.60 g of fragmented shale and 0.03–0.05 g of slivered graphite (to control oxygen fugacity during heating) were added to capsules, which were then sealed via cold-welding under normal atmospheric conditions. For anoxic heating, samples were loaded in an anoxic chamber (99.5% N_2 and 0.5% H_2), with 0.50–0.60 g of fragmented shale and 0.10–0.17 g of 10-μm sieve reduced iron powder (Fe^0; to control oxygen fugacity) added to capsules and subsequently cold-welded while still within the anoxic chamber. It was expected that at run temperature and pressure, the Fe metal would react with any oxygen in the capsule to form FeO (wüstite) and control the oxygen fugacity along the Fe^0/wüstite equilibrium curve. While the masses of the included components for oxygen fugacity control may seem dramatically different, the volumes are nearly identical (ranging from 0.013 to 0.022 cm^3, calculated with densities of 2.23 g cm^{-3} [graphite] and 7.874 g cm^{-3} [iron]). The choice of different oxygen fugacity-controlling components is directly related to ease of post-heating removal. Whereas graphite slivers were hand-picked with forceps under reflected light microscopy, the iron powder could be easily removed with a magnet. However, the rapid oxidation of reduced iron powder with exposure to oxygen made it a less suitable oxygen fugacity-controlling agent in experiments run under oxic conditions.

After the capsules were sealed, the pre-heating masses were recorded, and they were placed in individual cold-seal pressure vessels. The temperature of the furnace was maintained at 500 ± 2.5 °C (at standard atmospheric pressure) for the duration of the heating term. The capsule number, preparation method (oxic or anoxic), time-in, time-out, and pre-heat mass were recorded for each of the furnaces and pressure vessels. The oxic capsules were heated for varying lengths of time up to 2 weeks (one capsule each for the durations of 1, 3, and 5 days; two capsules each for 7, 10, and 14 days), and the anoxic capsules were heated for up to 250 days (one capsule each for 5, 125, and 250 days)—this discrepancy in heating duration vs. preparation mode will be further discussed in section 'Initial observations'. Once the pressure vessels were removed from the furnace, the capsules were retrieved, weighed, opened, and cleaned with a fine-tipped paintbrush to ensure complete removal of all material. The rock fragments and oxygen fugacity-controlling component extracted from each capsule were stored in individual Nalgene® acid-resistant Petridishes, which were examined using optical microscopy to again check for the presence of acritarchs, and oxygen fugacity-controlling agents were removed. The remaining post-heating rock material was subsequently macerated with reagent-grade (48–51%) hydrofluoric acid for 12 h. As the 1.2 g of unheated shale yielded approximately 60 acritarchs, we attempted to extract a minimum of 20 acritarchs per 0.5–0.6 g of heated sample (usually with 5–10

acritarchs remaining within the macerate residue). The extracted specimens were rinsed in distilled-deionized water to remove any debris and hydroflouric acid residue and were then mounted on pre-labeled, standard glass microscopy slides. All of the mounted specimens were then examined via optical microscopy for thermal alteration scoring and Raman spectroscopy. Following this examination, three specimens from each heating experiment were separated and prepared for XPS analyses, and five additional specimens were prepared for SEM analyses.

Optical microscopy, thermal alteration scoring, and digital photomicrograph analysis

To examine any physical changes in the acritarchs after heating, we devised thermal alteration scoring systems as detailed below to evaluate opacity and reflectivity; these recognizable properties are directly related to visible characteristics of kerogenous materials known to have undergone carbonization or graphitization. These scoring systems were devised based on the 10 unheated baseline acritarchs previously extracted from a separate SYG sample rather than those comprising the control acritarchs in an effort to be unbiased in the scoring of control acritarchs. This mode of assessing thermal alteration through fossil scores is labeled throughout the text as the opacity index (*Oi*) and reflectivity index (*Ri*). After thorough inspection of the baseline group acritarchs, the control and treatment replicates were initially scored by J.D.S. and independently verified by a third party (J.W. Huntley) provided with a detailed description of score assessments and photographic references (Fig. 1). Joint reexamination resolved the discrepant scores (6 of 358 total values, all of which occurred in the *Oi* assessments; see full data table in Appendix A). Representative optical photomicrographs from each heating experiment are shown in Fig. 2.

For quantification of the *Oi*, we examined the extracted acritarchs using transmitted light microscopy (Olympus BX51-POL petrographic microscope, Olympus, Center

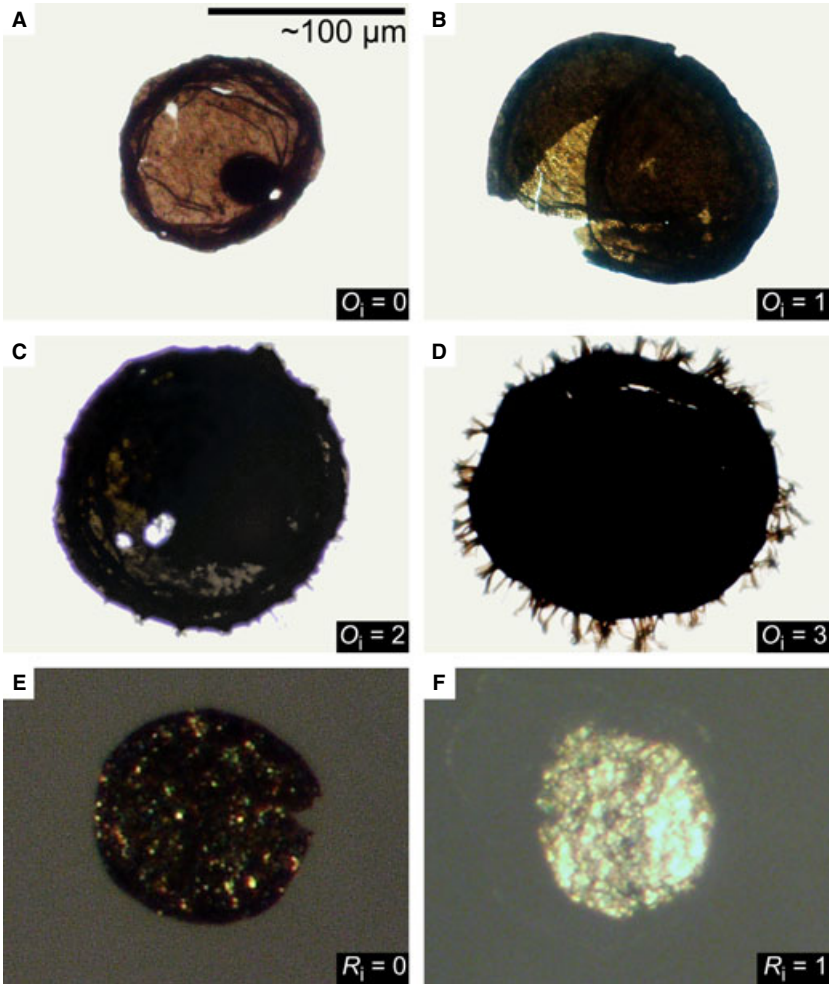

Fig. 1 Opacity (*Oi*) and reflectivity (*Ri*) index score reference examples from control group acritarchs. (A–D) *Oi* score classifiers, 0–3 respectively. (E–F) *Ri* score classifiers, 0–1 respectively.

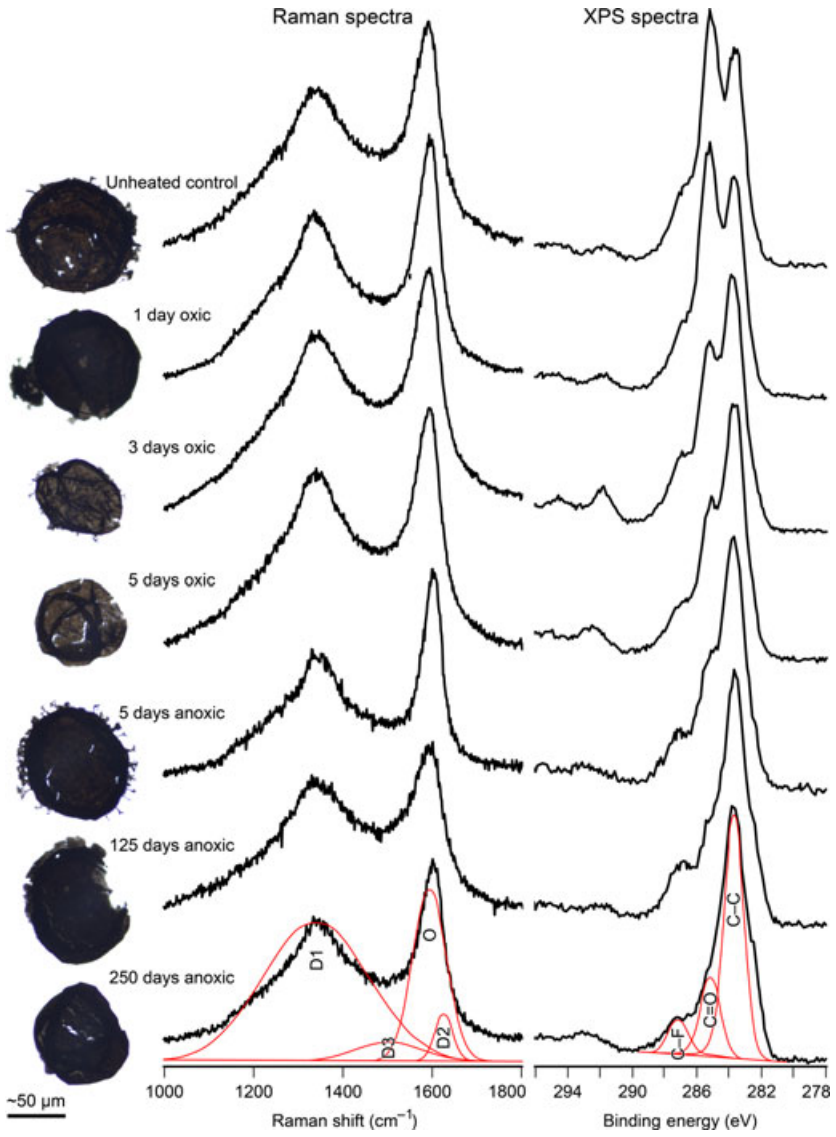

Fig. 2 Representative optical photomicrographs, Raman spectra, and XPS spectra from each experimental group (and the unheated control group). For each of the represented spectra, the spectrum with values closest to the average values for each group was selected. In addition, a generalized peak fitting (with peaks labeled) is shown in the 250 day anoxic spectra.

Valley, PA, USA) with a constant light intensity throughout the assessment. Each acritarch was scored on a four point scale (0–3), in which higher scores indicate a more opaque acritarch and lower scores indicate greater transparency. To maintain consistency, the *Oi* was gauged from regions of the acritarch where the two vesicle walls clearly overlapped, rather than from compression folds with multiple overlapping layers of vesicle walls or from fragmented regions with only one vesicle layer. The *Oi* point scale can be described as follows: 0 = acritarchs that were highly transparent, with no opaque regions where two vesicle walls overlapped; 1 = acritarchs that showed opaqueness in approximately 1–49% of the total surface area where two vesicle walls overlapped; 2 = acritarchs that were ≥ 50% opaque, but still exhibited regions of transparency; and 3 = acritarchs that were entirely opaque (Fig. 1A–D).

Gradational color change of kerogenous material—ranging, in a stepwise fashion, from yellowish-amber to black with increasing thermal maturity—has been well established (Gutjahr, 1966; Staplin, 1969; Peters *et al.*, 1977; Batten, 1996). However, rather than color, opacity was chosen as the primary gauge to assess thermal maturity because the acritarchs chosen for this study already possess a baseline thermal alteration index (TAI; Batten, 1996) of 3–4, with a corresponding color of orange-brown to dark brown, as assessed by Marshall *et al.* (2005). As a confirmatory technique to assess the reliability of the scoring system and to evaluate potential variation in color, 8–10 acritarchs were randomly

selected from each replicate group and digitally photographed using a Lumenera Infinity digital camera attached to an Olympus BX51 transmitted light petrographic microscope, with uniform lighting conditions. Following the method described in Schopf *et al.* (2005), red, blue, and green (RBG) values were assessed using Adobe Photoshop CS4® for the enumeration of acritarch color. A total of 20 RGB color values were recorded from randomly selected regions of each acritarch. If the specimen contained regions of variable coloration, then 10 measurements were randomly taken in the darker color region and 10 from the lighter color region. Each set of RGB values was then converted to a percent value (by normalizing total intensity to 100%). The values are reported here as R:B ratios only, because G percentages were highly consistent across all measurements at 30.08 ± 0.05%). In Schopf *et al.* (2005), the well-known color gradient of kerogenous material has been quantified and defined in terms of the R:B ratio: R:B > 2.0 corresponds to amber-brown; R:B = 2.0–1.5 corresponds to brown; R:B = 1.4–1.0 corresponds to dark brown; R:B = 0.9–0.5 corresponds to brownish-black; and R:B < 0.5 corresponds to black. Because our samples had already experienced natural thermal modification, we anticipated that our analyses would illustrate a much narrower range than that reported by Schopf *et al.* (2005), although we were optimistic that lower R:B ratios would correspond to more opaque regions and higher ratios to more transparent regions.

In studies of Phanerozoic sedimentary organic matter, vitrinite reflectance (usually abbreviated as R_0 or VR) has been a key method for constraining thermal maturity and temperature history of hosting sediments (Senftle & Landis, 1991; Marshall *et al.*, 2005). R_0 measurements are dependent on the presence of vitrinite, a component of higher plant-derived Type III kerogens (i.e., woody tissues; Vandenbroucke & Largeau, 2007). While clearly the Mesoproterozoic Ruyang samples used here appreciably predate the evolutionary appearance of higher plants, and their carbonaceous material is predominately Type I kerogen alginite macerals of a microbial or algal origin (Vandenbroucke & Largeau, 2007), equivalent R_0 values can be assessed from older carbonaceous materials. Indeed, from previous examination of the Ruyang acritarchs, Marshall *et al.* (2005) assigned an approximate equivalent R_0 of 0.5–0.75 based on their TAI assessment. However, normal methods of measuring R_0 require polished specimens, which was not preferable with our experimental approach because of the small volumes of powdered/crushed material as well as the analytical protocol for macerating and extracting acritarch specimens. These complications necessitated a different approach; thus, a second scoring system was devised to quantify the percent reflectivity of each treatment group (reflectivity index, or *R*i). This index is a modified presence–absence scoring system, and scores were assigned using reflected light microscopy (Olympus SZ11 stereomicroscope, Olympus, Center Valley, PA, USA) with a constant light intensity and angle. Because these acritarchs have a baseline equivalent R_0 before being heated, the post-treatment acritarchs were evaluated against the baseline acritarchs and scored either a 1 for more reflective or a 0 for equally reflective as compared to the average unheated baseline acritarch (Fig. 1E–F). At the onset of *R*i data assessment, this index was devised on a 0–2 scale because, hypothetically, a heated acritarch may have been less reflective than the average unheated baseline acritarch, which would have received the initial 0 score. No such instance was observed in our replicates, and therefore, the scale was adjusted to the standard presence–absence scoring scheme of 0–1, which when averaged can be viewed simply as a percentage of acritarchs per replicate group that are more reflective than the baseline group.

Raman spectroscopy

Raman spectroscopy is an effective tool for assessing the degree of crystallinity in carbonaceous materials—notably of extracted kerogens such as those reported herein—as poorly ordered kerogen and well-ordered graphite produce differing Raman shifts (Pasteris & Wopenka, 1991, 2003; Jehlička & Bény, 1992, 1999; Wopenka & Pasteris, 1993; Yui *et al.*, 1996; Jehlička *et al.*, 1997, 2003; Spotl *et al.*, 1998; Nestler *et al.*, 2003; Marshall *et al.*, 2010). Further, the degree of crystallinity of carbonaceous material has been shown to correlate strongly with the peak metamorphic temperature that it experienced (Grew, 1974; Pasteris & Wopenka, 1991; Wopenka & Pasteris, 1993; Beyssac *et al.*, 2002a, 2003). The principal Raman spectral characteristics of carbonaceous materials in the first-order region (e.g., Tuinstra & Koenig, 1970; Bény-Bassez & Rouzaud, 1985; Jehlička & Bény, 1992; Wopenka & Pasteris, 1993; Schopf *et al.*, 2005) are known as the disordered (D) and ordered (O, sometimes labeled as graphitic, or G) bands, which center, respectively, at approximately 1350 and 1580 cm^{-1}. Generally, the primary D band (also known as the D1 or defect band) is produced by disordered sp^2 carbon, specifically in-plane defects and heteroatoms, corresponding to structural deviations of carbonaceous materials from crystalline graphite. In hydrocarbon-dominated carbonaceous materials, the D band is composed of numerous subsidiary bands, but these disappear in the symmetric D band observed in well-ordered graphitic (hydrogen-poor) material. A sharp and narrow O band observed in graphite indicates well-ordered crystalline carbon. On the other hand, a broad O band, apparent in disordered graphite and carbonaceous materials, represents the amalgamation of two non-resolvable peaks, including the ordered peak at 1580 cm^{-1} and a disorder-induced shoulder (D2 band) positioned at approximately 1620 cm^{-1}, producing a single band centered at approximately 1600 cm^{-1}. The wide D3 band, centered at 1500 cm^{-1} and appearing only in very poorly ordered carbonaceous materials, has been attributed to defects outside the plane of aromatic layers.

In previous studies, the inverse relationship between D:O band intensity ratios (or $I_{\sim 1350\,cm^{-1}}/I_{\sim 1600\,cm^{-1}}$) or O peak widths (full width at half maximum intensity) and carbonaceous material crystallinity has served as a basis for assessing the intensity of metamorphic transformation (Tuinstra & Koenig, 1970; Pasteris & Wopenka, 1991; Jehlička & Bény, 1992; Wopenka & Pasteris, 1993). Numerous other metrics, such as $D/(O + D) \times 100$ and $D1/(O + D1 + D2)$ area ratios, have also been used for similar purposes (Wopenka & Pasteris, 1993; Beyssac *et al.*, 2002a,b, 2003). In 2005, Schopf *et al.* introduced and quantified a different metric to characterize thermal maturity of carbonaceous materials. They proposed the Raman Index of Preservation (RIP) based on experimentally heated Bitter Springs and Chichkan microfossils. These host-rock embedded microfossils were heated in a tube furnace at varying temperatures, ranging from 200 to 1200 °C, for a constant amount of time (2 h). The RIP metric specifically compares two parameters calculated from the D bands of Raman spectra as an index of thermal transformation of kerogenous materials. The α parameter estimates the contribution of the D band shoulder (centered at approximately 1270 cm^{-1}) to the area of the entire D band (1100–1500 cm^{-1}), expressed as a ratio of spectral areas between 1100–1300 cm^{-1} and 1100–1500 cm^{-1}. The γ parameter assesses the contribution of the graphitization-specific D band component (centered at approximately 1350 cm^{-1}) to the full D band area, expressed as a ratio of spectral areas between 1300–1370 cm^{-1} and 1100–1500 cm^{-1}. Therefore, a simplified RIP can be expressed as a spectral area ratio of the D band shoulder (1100–1300 cm^{-1}) to the graphitization-specific D band (1300–1370 cm^{-1}; Schopf *et al.*, 2005). The rationale behind this scheme is that, as temperature increases (up to 900 °C), the position of the D shoulder moves to higher wavenumbers and becomes subsumed by the D band proper, leading to lower RIP values.

To prepare our acritach specimens for Raman spectroscopic analysis, each extracted specimen was placed in a pre-positioned DD water droplet on a pre-labeled microscopy slide, and was held in place via static friction force upon evaporation of the water droplet. The specimens were then analyzed on a HORIBA JobinYvon LabRAM HR800 Raman microprobe equipped with a high-resolution 800-mm focal length spectrometer and an Andor electronically cooled charge-coupled device (CCD) detection system. All analyses presented herein used a LaserPhysics Reliant 100S-514 nm wavelength (green) argon laser oriented normal to the acritarch surface (as per Marshall *et al.*, 2010). In addition, as carbonaceous materials can be anisotrophic, Raman spectra were collected at different surface orientations (0 °, 90 °, 180 °, and 270 °) and showed negligible variation in D and O band intensities or spectral shape, indicating that polarization effects were not significant. The laser was focused to a ≤10 μm diameter spot with a 40× objective lens to collect backscattered radiation, and the final laser power was 1–3 mW on the sample to minimize laser induced photodamage. An acquisition time of 60 s was used, and the measured Raman shift was constrained between 1000 and 1800 Δcm^{-1} to focus only on the prominent kerogenous vibrational bands (representative Raman spectra shown in Fig. 2). Spectral baseline correction and deconvolution into four component Gaussian–Lorentzian bands (corresponding to the D1, D2, D3, and O bands, as shown in the spectrum for a 250 day anoxic specimen in Fig. 2) were conducted via FITYK 0.9.8 open-source software (Wojdyr, 2010). Following spectral baseline correction, integrations of peak areas for calculation of $D/(D + O) \times 100$ area ratios and RIP values, as well as assessments of peak heights for calculation of D:O peak intensity ratios were conducted in Microsoft Excel 2010 and double-checked in FITYK 0.9.8.

Statistical analyses

Quantitative data consisted of thermal alteration scores and Raman indices recorded for each specimen grouped by experimental treatment. The resulting data set was analyzed using SAS 9.2 and PAST 1.89 (Hammer *et al.*, 2001). Resampling techniques, including bootstrap or binomial confidence intervals and experiment-wise randomization simulations, were used to evaluate the statistical significance of *O*i and *R*i scores, D:O intensity ratios, and RIP values. As $D/(D + O) \times 100$ area ratios were highly consistent across groups (see Table 1 and Appendix A), these values were

Table 1 Optical and Raman-based thermal alteration indices

Heating duration (days)	Preparation	Acritarchs measured (*n*)	Mean *O*i (0–3)	Mean *R*i (0–1)	Mean D:O ± 1σ	Mean $D/(D + O)\times 100$ ± 1σ	Mean calibrated RIP ± 1σ
0	Control	50	1.30	0.12	0.68 ± 0.004	59.72 ± 0.08	8.29 ± 0.04
1	Oxic	24	1.79	0.33	0.67 ± 0.005	60.22 ± 0.06	8.49 ± 0.05
3	Oxic	25	0.96	0.28	0.70 ± 0.008	59.67 ± 0.16	7.77 ± 0.12
5	Oxic	19	0.74	0.26	0.70 ± 0.008	59.61 ± 0.13	7.97 ± 0.13
5	Anoxic	20	1.40	0.40	0.59 ± 0.006	59.26 ± 0.10	8.11 ± 0.05
125	Anoxic	20	1.75	0.55	0.76 ± 0.006	60.26 ± 0.08	8.04 ± 0.08
250	Anoxic	21	2.10	0.62	0.70 ± 0.013	59.93 ± 0.09	8.01 ± 0.08

Means (± standard error where applicable) for pertinent carbonization index or measurement (*O*i = opacity index, *R*i = reflectivity index, D:O = Raman peak intensity ratio, $D/(D + O) \times 100$ = Raman peak area ratio, RIP = Raman Index of Preservation) sorted by experimental group (heating duration and preparation).

excluded from bootstrapping and randomization statistical tests and are not represented graphically.

To estimate sample-wise confidence intervals for each experimental group, the ordinal *O*i scores, D:O ratios, and RIP values were bootstrapped (10 000 iterations, resampled with replacement) using a custom SAS/IML code in SAS 9.2. A balanced bootstrap algorithm, which ensures that the grand mean of bootstrap samples equals the actual sample mean, was employed here (see Kowalewski *et al.*, 1998; Kowalewski & Novack-Gottshall, 2010 for additional details). For each bootstrap simulation, an independent simulation of 10 000 iterations has been employed, and actual means, bootstrapped standard errors, and bootstrapped 95% confidence intervals were recorded. Pilot tests (not shown here) demonstrated that estimates of standard error stabilized well below 5000 iterations, indicating that a Monte Carlo approximation based on 10 000 iterations should be highly reliable. Because the *R*i alteration scores consisted of presence–absence data, 95% binomial confidence intervals were calculated in place of bootstrapped confidence intervals.

To assess statistical significance of differences between experimental groups, randomization methods have been employed. Randomization, a resampling strategy based on random reassignment (without replacement) of observations across groups (specimens across experimental groups in our case), is a well-understood resampling strategy developed specifically to evaluate experimental data (e.g., Edgington & Onghena, 2007; Kowalewski & Novack-Gottshall, 2010). Iterative resampling, under a given randomization protocol, allows for generating an empirical approximation for a probability density function of a statistical parameter of interest (e.g., a sample mean computed from experimental data). In the specific case of this study, two different metrics have been used to evaluate statistical significance of the data produced in the heating experiments. The first metric used, referred to as Cumulative Difference (CD), is a cumulative difference in a parameter of interest across the experimental replicates grouped by heating duration. For example, mean *O*i values for the oxic experimental group, at 1, 3, and 5 days of heating, were 1.79, 0.96, and 0.74, respectively. Consequently, CD = (1.79 − 1.30) + (0.96 − 1.79) + (0.74 − 0.96) = −0.56, where 1.30 is the mean *O*i for the unheated control group. This metric indicates a cumulative decrease in *O*i of 0.56 between the unheated control group (1.30) and the group heated for the longest time interval (0.74). In a randomization model, specimens from all experimental groups (including the unheated group) were randomly reassigned across groups, while retaining the original sample size, and a value of CD (CD_R) was computed at each iteration. Because randomized groups are assembled by sampling all specimens randomly, the resulting random groups vary in CD stochastically and the mean CD_R converges on zero. By comparing the observed CD value against the sampling distribution of CD_R values, a statistical significance (probability of experimental CD value being produced by random chance) can be estimated, effectively evaluating the magnitude of change across the experiment.

In addition to CD, a more conservative rank-based parameter was used. Referred to as cumulative sign difference (CSD), this parameter is simply computed as a cumulative sum of rank differences across experiments. For example, if a value of a parameter is lowest for the unheated control group (rank = 1), intermediate for the 'short-term heating' group (rank = 2), higher intermediate for the 'moderate-term heating' group (rank = 3), and highest for the 'long-term heating group' (rank = 4), CSD is three because the sign differences between successive heating durations are all positive. This is the case, for example, with the mean *O*i for the anoxic experimental group (with values of 1.40, 1.75, and 2.10 for 5, 125, and 250 days, respectively). For the oxic group *O*i, however, only the sign difference between the control and 1 day duration is positive; the sign differences between 1 and 3 day groups and between 3 and 5 day groups are negative, resulting in a CSD of −1. As in the case of CD, random values of CSD (CSD_R) can be computed iteratively using the above randomization protocol and the mean CSD_R value is expected to converge on zero. Again, by comparing the observed CSD value to the sampling distribution of CSD_R values, statistical significance can be estimated, but in this case, evaluating the direction of change across the experiment.

For each parameter and experiment, a randomization protocol was run 10 000 times and the resulting distribution was used to estimate the significance value *P*. The *P* value was estimated as proportion of CD_R or CSD_R values that equaled or exceeded the CD or CSD value actually observed in the experiment. Pilot tests (not shown here) demonstrated that estimates of standard error stabilized well below 5000 iterations indicating that a Monte Carlo approximation based on 10 000 iterations should be highly reliable. All simulations were written in SAS/IML.

X-ray photoelectron spectroscopy

X-ray photoelectron spectroscopy is a relatively underutilized tool in the characterization of fossil carbonaceous materials, with only a few case studies (e.g., Butterfield, 1996; Marshall *et al.*, 2001; Toporski *et al.*, 2002; Schweitzer *et al.*, 2008). XPS instruments are primarily utilized for quantitative analysis of elemental composition and chemical bonding states within the top few nanometers of a surface (e.g., near surface composition measurements in a range of solid materials such as polymers and metals) and are useful in the identification of the nature of carbon bonds (Stipp & Hochella, 1991; Butterfield, 1996). XPS bombards a sample surface with X-rays (typically Al K_α) and measures the energy of the emitted photoelectrons (Vickerman & Gilmore, 2009). The

low energy of the emitted photoelectrons (generally <1100 eV) results in a small escape depth for these electrons (typically <10 nm), which gives this technique its high surface sensitivity. The energy of the emitted photoelectrons is influenced by the local chemical bonding environment, allowing XPS to discern differences in bonding. For instance, binding energy shifts observed in this study (C–C vs. C=O vs. C–F) are caused by the more electronegative element (electronegativity is F>O>C) pulling electrons away from the carbon, causing carbon to bind its remaining electrons more tightly. This results in a shift of the photoelectron energy to higher binding energies depending on the element to which the C is bound.

Three specimens from each heat treatment group (five from the unheated control group) were selected for XPS analysis, using a PHI Quantera SXM system equipped with a highly focusable scanning monochromatic X-ray source (beam size <9 μm; representative XPS spectra shown in Fig. 2). The specimens were randomly chosen, removed from the microscopy slides, and again rinsed in DD water to remove any potential contaminants. They were then static-mounted to pre-labeled 1 cm^2 glass slides.

X-ray photoelectron spectroscopy spectra were analyzed via CasaXPS ver. 2.3.14 software, in which each of the three peaks between binding energies 283 and 288 eV were fit (using a Gaussian-Lorentzian fitting method; an example of peak fitting shown in Fig. 2) and percent areas were assessed. The three peaks are positioned at 283.7, 285.24, and 286.98 eV, with the full width at half maximum height ≤1.4 eV for all peak fits. These three peaks correspond to condensed aromatic carbon rings (referred to here as 'graphite-like' carbon; C–C), aldehydes and ketones (C=O), and fluorocarbon (C–F) maceration contaminants, respectively (Wagner *et al.*, 1979).

Scanning electron microscopy

Five randomly chosen specimens from each heat treatment group were selected for surficial morphological analysis via SEM. The specimens were prepared identically to those prepared for XPS analyses. The pre-labeled 1-cm^2 glass slides were subsequently affixed to standard aluminum SEM stubs with pre-cut carbon tape discs. A thin strip of conductive carbon tape was affixed to the top of the slide and the lower surface of the aluminum stub to create a conductive bridge aiding in charge dispersal. The stub-hosted slides were sputter-coated with a 5-nm-thick gold–palladium coating in a Cressington 208HR sputter coater with an MTM-20 thickness controller. Surficial analyses were conducted in an FEI Company Quanta 600 field-emission environmental SEM in high vacuum mode with a 10 keV accelerating voltage, 2.0 spot size [probe diameter/beam current], and a 14.5-mm working distance. Secondary electron imaging was conducted with an Everhart–Thornley detector.

RESULTS AND DISCUSSION

Initial observations

Initial observation of rock fragments recovered from heating experiments clearly indicated signs of thermally induced alteration. Firstly, acritarchs exposed on heated fragment surfaces were typically more easily identifiable because of their darker coloration than those on fresh, unheated shale chips. Secondly, there appears to be a bias in preservation, or more aptly survivability, of acritarchs in the two differing capsule preparation modes. In samples heated under oxic conditions for a week or more, the initial reflected light microscopic observation of the recovered rock fragments showed appreciably fewer acritarchs compared with fragments that were heated for a shorter duration or those that were prepared in anoxic conditions. Indeed, acid digestion of heated rock fragments confirmed that acritarchs survived for a maximum of 5 days of heating within capsules prepared under oxic conditions, substantiated by failure to yield extractable acritarchs from multiple heating runs beyond 5 days (six total runs: two runs each at 7, 10, and 14 days; the probable cause for which will be further discussed in section 'Scanning electron microscopy'). In contrast, in all cases prepared in anoxic conditions, at least 20 acritarchs (with 5–10 acritarchs remaining in the macerate residue) were extracted from each capsule, even after 250 days of heating. In general, the morphologies of the acritarchs were retained in both atmospheric settings, and no obvious features related to graphite crystal growth (such as hexagonal crystal overgrowth) were observed. In the capsules prepared under oxic conditions, however, extracted acritarchs seemed to be more fragile during sample handling than those removed from either the unheated control shales or the capsules prepared under anoxic conditions.

Thermal alteration scoring and digital photomicrograph analysis

The thermal alteration scoring system illustrated a general trend of increasing opacity and reflectivity in the acritarchs recovered from the anoxic capsules, but no consistent trend in acritarchs subjected to oxic preparation. The control acritarchs yielded a mean *O*i score of 1.30 (corresponding to mostly transparent acritarchs) and mean *R*i of 0.12. To resolve potential confusion of *R*i scores for the control group, it is important to reiterate that the score classifiers were assessed from a subset of 10 baseline acritarchs that were not part of the control group; therefore, a *R*i score of 0.12 for the control group indicates that 6 of the 50 control acritarchs were judged to be more reflective than the 10 baseline acritarchs. The oxic capsule acritarchs had an initial increase in both mean *O*i and *R*i scores after 1 day of heating, but then showed subsequent declines after both 3 and 5 days, with the mean *O*i score at both heating durations dropping below that

of the unheated control acritarchs (reaching minimum mean values of 0.74 [*Oi*] and 0.26 [*Ri*]; Fig. 3A–B, Table 1). Acritarchs from anoxic capsules, on the other hand, showed a sustained increase in both thermal alteration indices over the course of the experiment, with *Oi* increasing linearly and *Ri* escalating rapidly between the control and 5 day span followed by minor incremental increases at the 125 and 250 day marks (reaching maximum mean values of 2.10 [*Oi*] and 0.62 [*Ri*]; Fig. 3C–D, Table 1).

The resampling CD test for *Oi* scores from the oxic replicates is significant at $\alpha = 0.05$, with a *P* value of <0.01; however, the CSD test did not show a significant directional trend in the *Oi* data, with a *P* value of 0.48. *Ri*, on the other hand, was not significant in either resampling test, with a CD $P = 0.10$ and a CSD $P = 0.47$. For the anoxic replicates, both indices show statistical significance in both resampling techniques, with CD test *P* values <0.01 and the CSD test *P* values ≤0.02 (Table 2).

Table 2 Cumulative difference (CD) and cumulative sign difference (CSD) resampling tests. Results displayed by index and preparation mode

Index	Preparation	CD	*P*	CSD	*P*
Oi	Oxic	−0.56	<0.01	−1	0.48
Oi	Anoxic	0.80	<0.01	3	0.02
Ri	Oxic	0.14	0.10	−1	0.47
Ri	Anoxic	0.50	<0.01	3	0.01
D:O	Oxic	0.02	<0.01	−1	0.50
D:O	Anoxic	0.02	0.08	−1	0.50
RIP	Oxic	−0.32	<0.01	1	0.50
RIP	Anoxic	−0.27	<0.01	3	0.03

The confirmatory R:B color index illustrated a strong negative correlation with the *Oi* scoring system ($R^2 = 0.86$), that is, lower *Oi* scores correspond to higher R:B values. In fact, each *Oi* score can be defined by a non-overlapping range of R:B values as follows: *Oi* = 0, R:B > 1 (observed range = 1.01–1.21); *Oi* = 1, 0.8 < R:B < 1 (observed range = 0.83–0.96); *Oi* = 2, 0.7 < R:B < 0.8 (observed range = 0.70–0.77); and *Oi* = 3, R:B < 0.7 (observed range = 0.59–0.67; Fig. 4A, Table 3). When the R:B values are organized by heating period and preparation method, their trends follow similar paths as those of the *Oi* scoring, as would be expected even though the R:B calculations were conducted on a randomly selected subset of the *Oi*-scored acritarchs (Fig. 4B–C, Table 4).

Kerogen color and vitrinite reflectance are commonly used metrics by paleontologists and organic geochemists alike in the assessment of thermal maturity of fossil organic materials (e.g., Peters *et al.*, 1977; Senftle & Landis, 1991; Batten, 1996; Hunt, 1996; Vandenbroucke, 2003; Marshall *et al.*, 2005; Schopf *et al.*, 2005). By using both the R:B ratio (*sensu* Schopf *et al.*, 2005) and the highly interrelated opacity index, we have demonstrated that the acritarchs prepared in anoxic capsules and heated at 500 °C for varying durations up to 250 days exhibit statistically significant trends. These trends include a linear increase in opacity, and correspondingly a darkening in color—although the mean R:B values were contained within a single color bracket (brownish-black,

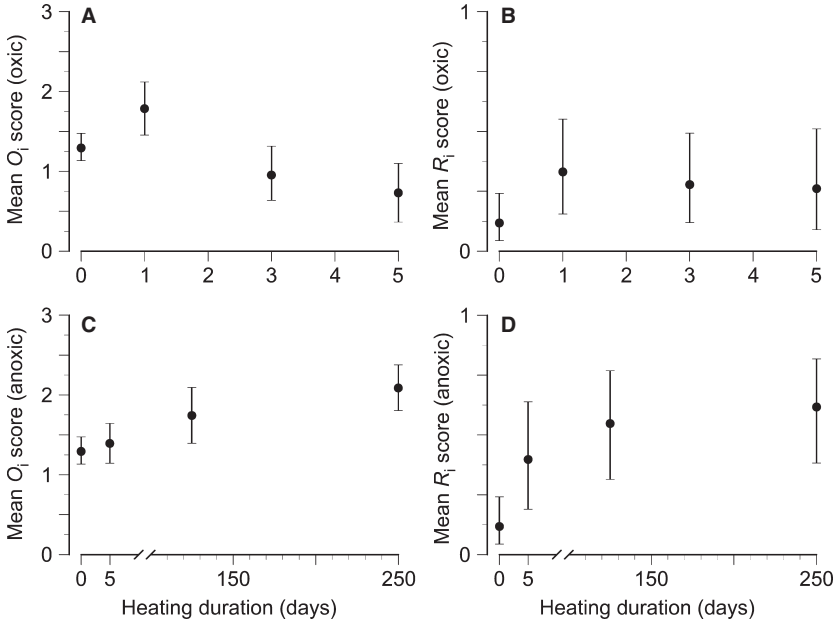

Fig. 3 Opacity (*Oi*) and reflectivity (*Ri*) index mean trends. (A) Mean oxic-preparation *Oi* scores with bootstrapped 95% confidence intervals. (B) Mean oxic-preparation *Ri* scores with 95% binomial confidence intervals. (C) Mean anoxic-preparation *Oi* scores with bootstrapped 95% confidence intervals. (D) Mean anoxic-preparation *Ri* scores with 95% binomial confidence intervals.

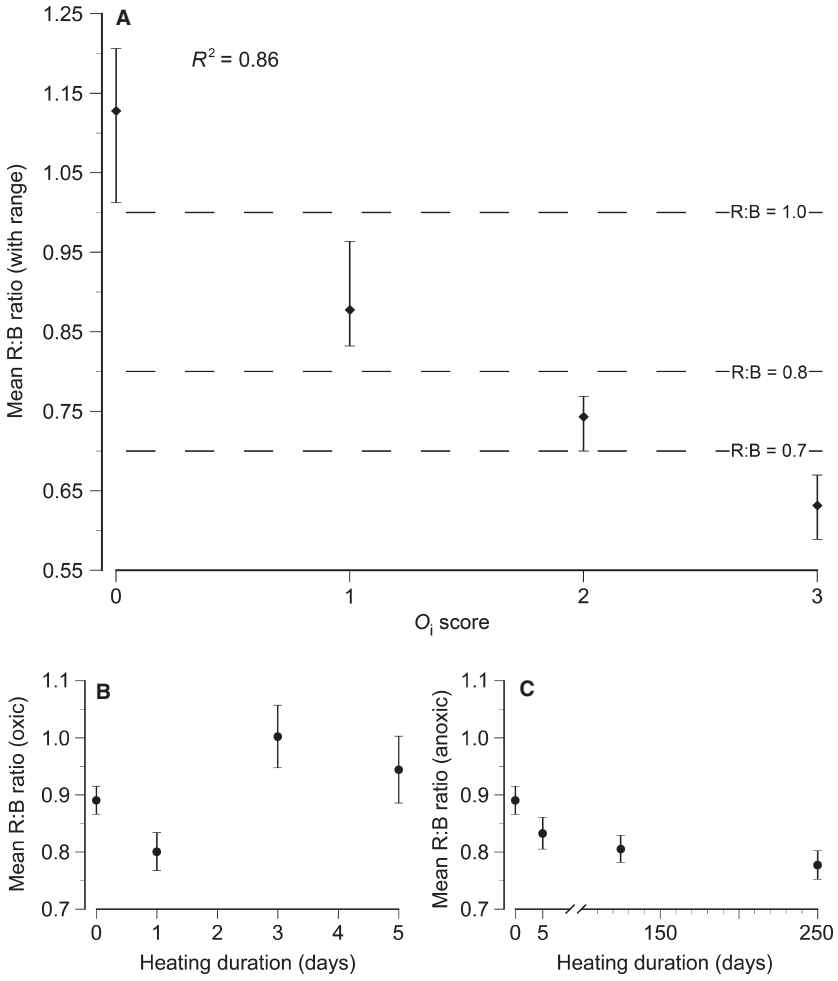

Fig. 4 Opacity index (*Oi*) vs. red:blue color ratio (R:B) and R:B mean trends. (A) *Oi* scores vs. mean R:B. Color ratio ranges (maximum and minimum values) indicated by bars around mean. Vertical dashed lines denote non-overlapping ranges of R:B values corresponding to *Oi* scores: *Oi* = 0, R:B > 1; *Oi* = 1, 0.8 < R:B < 1; *Oi* = 2, 0.7 < R:B < 0.8; and *Oi* = 3, R:B < 0.7. R^2 calculated from full R:B vs. *Oi* data set. (B) Mean oxic-preparation R:B ratio ± standard error. (C) Mean anoxic-preparation R:B ratio ± standard error.

Table 3 R:B ratios vs. *Oi* scores. Mean R:B ratios (± standard error) sorted by corresponding *Oi* score

Oi score	Acritarchs measured (*n*)	Mean R:B ± 1σ	Minimum R:B	Maximum R:B
0	9	1.13 ± 0.02	1.01	1.21
1	37	0.88 ± 0.01	0.83	0.96
2	17	0.74 ± 0.01	0.70	0.77
3	4	0.63 ± 0.02	0.59	0.67

R:B = 0.9–0.5) as proposed by Schopf *et al.* (2005). Thus, it may be important to note that there are indeed gradational changes within the color categories as initially proposed, which may become more important when examining comparable fossil taxa from similar deposits with slightly different thermal histories. In addition, the reflectivity of the acritarchs prepared under anoxic conditions illustrates a hyperbolic increase, with a high initial slope that decreases over time. Both *Oi* and *Ri* for the anoxic replicates display statistically significant trends, both in terms of magnitude (CD) and direction (CSD). However, the oxic replicates seemingly show no observable, or at least detectable, trend by these methods; the likely cause can be attributable to accelerated thermal degradation of the carbonaceous material in the presence of oxygen—as will be discussed in more detail in section 'Scanning electron microscopy'.

Raman spectroscopy

Three metrics related to microchemical transformation of kerogenous material were quantified from Raman spectra: D:O peak intensity ratio, D/(D + O) × 100 area ratio, and the RIP (Schopf *et al.*, 2005). The unheated control group acritarchs yielded a mean D:O ratio of 0.68. Over time with increasing carbonization, we would anticipate the D:O ratio, following an initial increase, to decrease from this control

Table 4 R:B ratios vs. experimental treatments. Mean R:B ratio (± standard error) sorted by acritarch experimental group (heating duration and preparation mode)

Heating duration (days)	Preparation	Acritarchs measured (*n*)	Mean *Oi* score	Mean R:B ± 1σ	Minimum R:B	Maximum R:B
0	Control	10	1.30	0.89 ± 0.02	0.70	0.96
1	Oxic	10	1.79	0.80 ± 0.03	0.59	0.94
3	Oxic	10	0.96	1.00 ± 0.05	0.73	1.21
5	Oxic	8	0.74	0.94 ± 0.06	0.71	1.15
5	Anoxic	9	1.40	0.83 ± 0.03	0.70	0.94
125	Anoxic	10	1.75	0.81 ± 0.02	0.63	0.87
250	Anoxic	10	2.10	0.78 ± 0.03	0.64	0.87

mean (Ferrari & Robertson, 2000). The acritarchs from the groups run under oxic conditions did show an initial decline in mean D:O at 1 day of heat treatment (0.67), but then an increase to 0.70 for 3 and 5 days of heat treatment (Fig. 5A, Table 1). The acritarchs run under anoxic conditions again showed an initial decline in D:O after 5 days of heating (0.59), a subsequent positive D:O change at 125 days (0.76), and a second decline at 250 days (0.70; Fig. 5B, Table 1). While both preparation modes were either significant or marginally significant via the CD test, with P = <0.01 for oxic replicates and 0.08 for anoxic replicates, neither preparation mode was statistically significant using the CSD test, with P values in both cases at 0.50 (Table 2).

The D/(D + O) × 100 area ratios were highly consistent across the unheated control acritarchs as well as all experimental groups, for both oxic and anoxic preparation methods. Indeed, the mean D/(D + O) × 100 area ratios are mostly confined to a narrow range of 59–61 (full range = 57.97–61.36; Table 1, Appendix A), falling well within the standard kerogen range reported by Wopenka & Pasteris (1993).

The mean calibrated RIP values for the oxic groups show an initial positive trend from the unheated baseline RIP (8.29) after 1 day of heating (8.49). The following treatments of 3 and 5 days yielded first a decrease followed by a subsequent increase of RIP values (7.77 and 7.97), essentially mirroring the pattern observed in D:O (Fig. 6A, Table 1). The RIP values from the anoxic groups, however, do not inversely follow their corresponding D:O pattern and instead show a consistent, albeit slight, decrease with duration of heating (Fig. 6B, Table 1). For RIP, the CD test for both preparation groups resulted in a significant P value of <0.01, but only the anoxic CSD test was significant (P = 0.03 [anoxic] and 0.50 [oxic]; Table 2).

Two of the three Raman-based quantifications of carbonaceous material thermal maturity used here, D:O peak intensity ratios (Wopenka & Pasteris, 1993) and RIP (Schopf *et al.*, 2005), produced intriguingly differing trends which were seemingly unrelated in anoxic replicates. Firstly, neither preparation mode showed a significant directional trend in D:O intensity ratios as shown by the CSD tests (Table 2). For the anoxic-preparation mode, the D:O intensity ratio was the only measurement not to show a significant directional trend. It has been noted from Raman characterization of carbonaceous

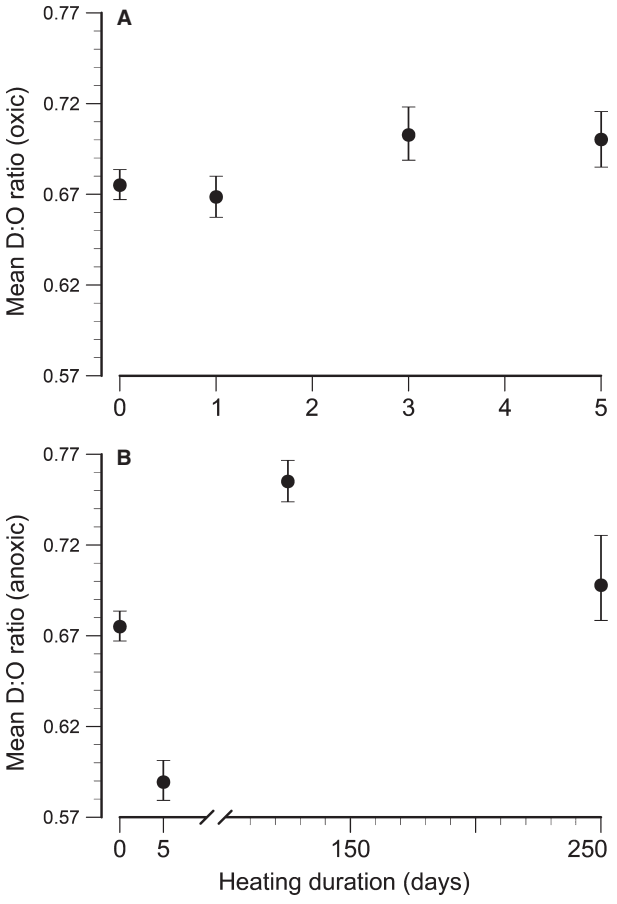

Fig. 5 Raman peak intensity ratio (D:O) mean trends. (A) Mean oxic-preparation D:O with bootstrapped 95% confidence intervals. (B) Mean anoxic-preparation D:O with bootstrapped 95% confidence intervals.

materials from varying metamorphic grades that breaks exist in the continuity of D:O intensity with increasing metamorphic grade (separated into metamorphic categories A, B, and C; see Pasteris & Wopenka, 1991 and Wopenka & Pasteris, 1993 for more details). In spite of this limitation, however, the D:O intensity ratio is a commonly used quantitative parameter for recognizing progressive carbonaceous material transformation via metamorphism, primarily sensitive to the degree of crystallinity of carbonaceous to graphitic materials (Wopenka & Pasteris, 1993; Pasteris & Wopenka, 1991,

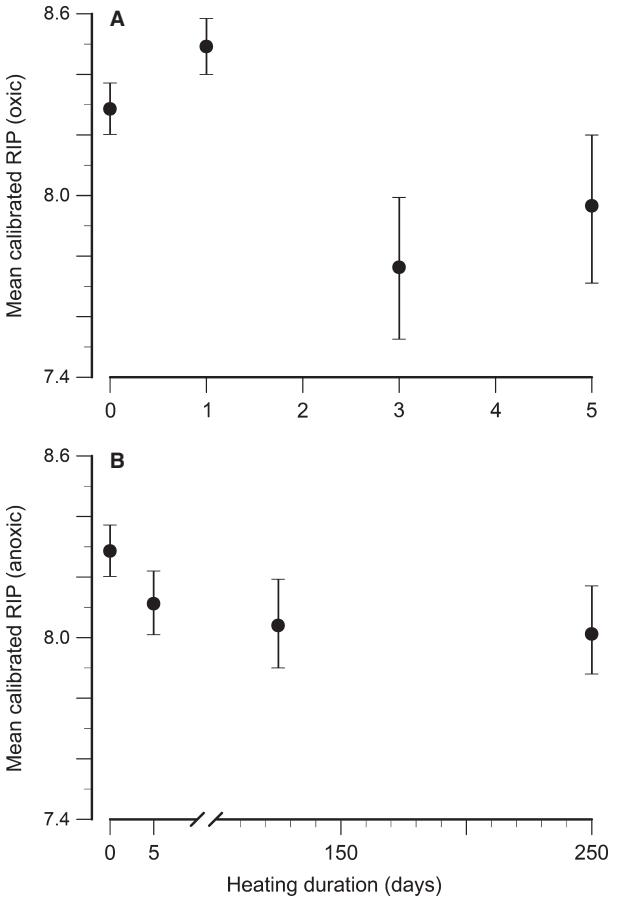

Fig. 6 Calibrated Raman index of preservation (RIP) mean trends. (A) Mean oxic-preparation RIP with bootstrapped 95% confidence intervals. (B) Mean anoxic-preparation RIP with bootstrapped 95% confidence intervals.

2002, 2003; Beyssac *et al.*, 2002b). Under uniform heating conditions, D:O ratios of samples from this study do not show a consistent trend of increasing carbonaceous ordering with increasing time, and D/(D + O) × 100 area ratios show uniform mean values across all experimental groups. If we assume that the acritarchs studied here are undergoing carbonization rather than graphitization through the duration of the experiment, we should expect the lack of trends observed with the D:O intensity and area ratio metrics. These metrics are not as reliable for kerogeneous materials undergoing carbonization and are instead more sensitive to the degree of structural ordering in graphitic materials (Wopenka & Pasteris, 1993). RIP values, on the other hand, may be more sensitive to changes in kerogenous materials undergoing carbonization, as they do show a significant variation in both magnitude ($P < 0.01$) and direction ($P = 0.03$) in samples from the anoxic capsules with increased heating duration. It is important to note, however, that following the largest RIP drop of 0.18 in anoxic heating, which occurred over the first 5 days of treatment, each of the mean RIP values between subsequent heating durations overlaps within ±1σ. Again, though, the oxic replicates do not show a significant directional trend in RIP, with fluctuation in mean values over the course of the experiment and an insignificant CSD test (Table 2).

X-ray photoelectron spectroscopy

X-ray photoelectron spectroscopy confirmed an increase in graphite-like carbon bonding (C–C) with duration of heating for both capsule preparation modes, with the anoxic capsules illustrating a slightly sharper increase. Correspondingly, as the C–C bond becomes a larger constituent, the aldehyde and ketone carbon bonds (C=O) showed a decline over the course of the experiment. Fluorocarbon (C–F) was formed as a contaminant from maceration using hydrofluoric acid and remained relatively constant in each group, comprising a mean of 11.87 ± 0.43% for all acritarchs analyzed (Table 5).

Surface sensitive XPS analyses confirmed that both preparatory procedures illustrated an increase in graphite-like C–C bonding and associated declines in aldehyde and ketone carbon bonding. The sample protocol, with replicates from each preparation mode undergoing 5 days of 500 °C heat treatment, allowed for direct comparison of XPS results between oxic and anoxic preparations. In this overlap duration, anoxic acritarchs did show a slightly higher (approximately 3%) measured C–C content than the oxic counterparts, potentially suggesting more complete carbonization in the absence of oxygen, although these values are not distinct beyond 1σ. However, with no acritarchs surviving oxic heating beyond 5 days, we could only observe further carbonization via the anoxic replicates, which reached a peak C–C content of nearly 70% at 250 days, approximately 25% higher than the unheated control acritarchs (Table 5).

Scanning electron microscopy

Observing sub-μm scale details of the acritarchs from each experimental group via SEM secondary electron imaging would shed light on any microstructural alterations experienced over the duration of the experiment (Fig. 7). For instance, as acritarchs heated under oxic conditions did not survive more than 5 days of heating at 500 °C, observing potential changes in microstructural details is an important step in determining the cause for their deterioration. Even after 1 day of heating, acritarchs from the oxic capsule showed microstructural alterations, such as disarticulation and degradation of the vesicle polygons (compare unheated acritarchs, Fig. 7A–B, with 1 day oxic heated acritarchs, Fig. 7C–D). More specifically, the reticulation ridges appear to have decomposed, rather than just splitting apart at the seams. This conclusion is based on the observation that numerous plates seemingly remain in place, but are separated by a few hundred nanometers, or approximately the size of the original plate boundary ridges. At 3 days (Fig. 7E–F) and 5 days (Fig. 7G–H), this trend not only

Table 5 Mean XPS carbon bonding percentages

Heating duration (days)	Preparation	Mean graphite-like carbon bonding (% C–C) ±1σ	Mean ketone/aldehyde carbon bonding (% C=O) ±1σ	Mean fluorocarbon contaminant bonding (% C–F) ±1σ
0	Control	44.79 ± 1.46	41.49 ± 1.87	13.72 ± 0.48
1	Oxic	44.84 ± 3.41	44.65 ± 3.44	10.51 ± 0.42
3	Oxic	50.97 ± 4.17	36.30 ± 2.20	12.72 ± 2.05
5	Oxic	56.48 ± 1.24	33.46 ± 1.68	10.07 ± 0.49
5	Anoxic	59.61 ± 4.48	28.81 ± 3.88	11.58 ± 0.65
125	Anoxic	64.35 ± 1.55	22.43 ± 1.07	13.21 ± 0.48
250	Anoxic	69.04 ± 1.76	20.94 ± 0.82	10.02 ± 1.07

XPS data, including mean condensed aromatic ring (graphite-like) C–C, ketone/aldehyde C=O, and fluorocarbon C–F bond percentages (±standard error), organized by acritarch experimental group (heating duration and preparation).

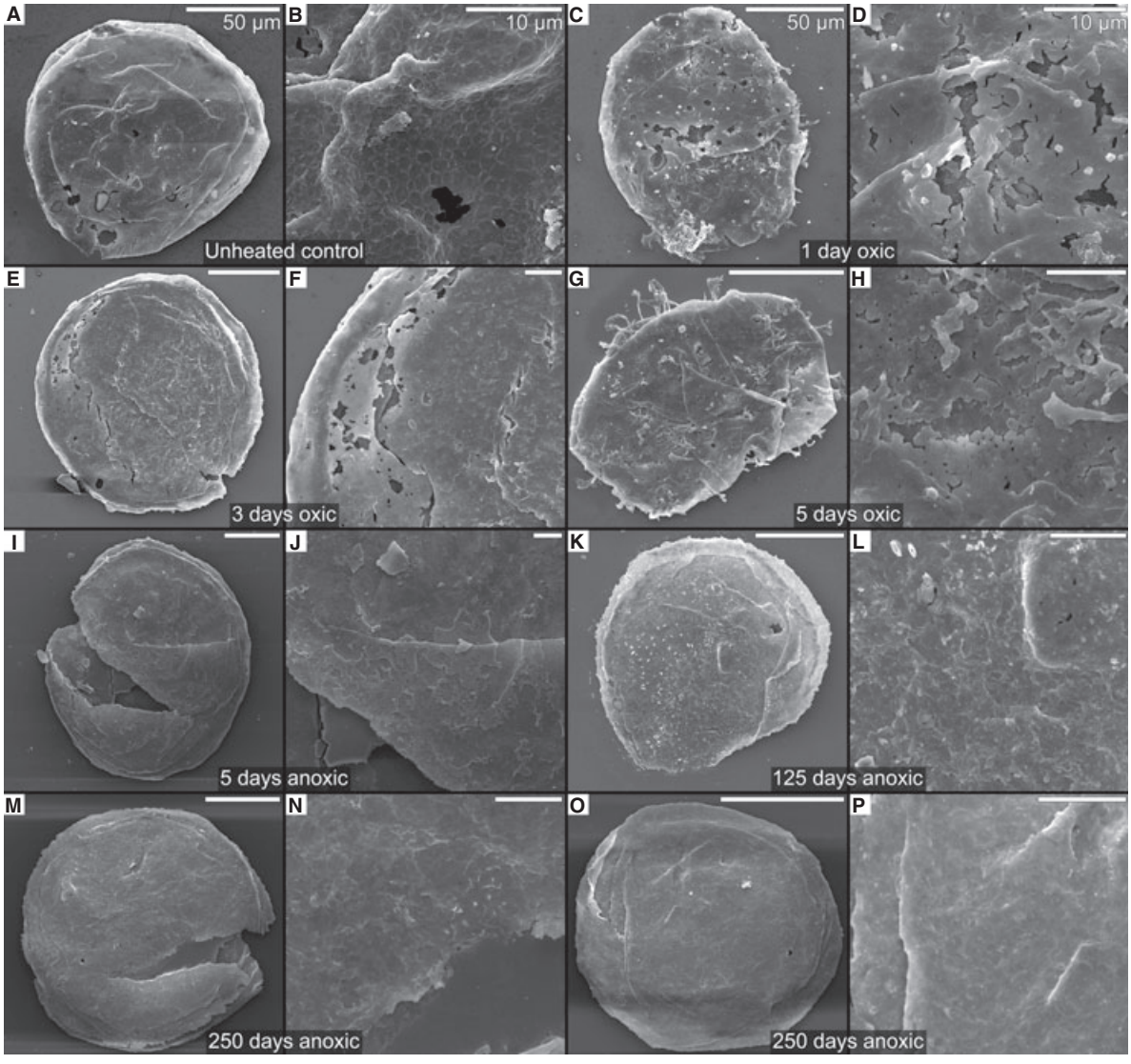

Fig. 7 Scanning electron microscopy secondary electron images of surficial microstructures. Each pair of images shows an overview (scale = 50 µm) and a magnified view (scale = 10 µm) of the same specimen. (A–B) Control group acritarch showing pronounced reticulation. (C–D) One-day oxic acritarch illustrating degradation of reticulations. (E–F) 3-day oxic acritarch with more advanced reticulation degradation. (G–H) 5-day oxic acritarch with pervasive reticulation degradation. (I–J) 5-day anoxic acritarch showing comparatively less degradation of reticulation than 5-day oxic acritarch example. (K–L) 125-day anoxic acritarch with much reduced reticulation, but preservation of structural integrity. (M–P) Two 250-day anoxic acritarchs with ghost relic reticulations visible in N and P and smooth inner vesicle surface visible in N (the inner surface has shown to bear reticulate cracks in ultrastructural studies; for instance see fig. 5E–J in Javaux *et al.*, 2004; and fig. 3D–E in Schiffbauer & Xiao, 2009).

continued but also became more pervasive across the surface of the samples imaged, with microcracks and fractures not related to excystment structures becoming more prevalent within the oxic replicates at longer heating durations. The decomposition of the reticulate ridges undoubtedly made the acritarchs more prone to fragmentation during acid maceration/extraction, which is likely in turn responsible for the lack of recoverable acritarchs beyond 5 days of oxic heating even though a few seemingly intact acritarchs were observed on pre-macerated rock fragments removed from capsules heated for 7 days in oxic conditions. The reticulate ridges have a texture similar to the plates, as shown in ultrastructural analyses via transmission electron microscopy and focused ion beam electron microscopy (Javaux *et al.*, 2004; Schiffbauer & Xiao, 2009); thus, some other mechanism must be responsible for this localized and seemingly selective thermal degradation. The cause of such localized corrosion remains to be determined, but we hypothesize that the raised reticulate ridges may have a higher surface area than the flat hexagonal plates allowing for more rapid thermochemical decomposition than the smooth plates. That is, the presence of oxygen likely accelerates degassing and disintegration, resulting in selective destruction of the reticulate ridges. Additionally, these reticulate ridges correspond to polygonal cracks on the interior surface of the vesicle (see fig. 5E–J in Javaux *et al.*, 2004; and fig. 3D–E in Schiffbauer & Xiao, 2009), which may also facilitate the cracking and fragmentation during heating.

In the acritarchs heated under anoxic conditions, on the other hand, the reticulate plate boundaries did not show the same evidence of deterioration, but instead seemed topographically reduced (Fig. 7I–P). The reticulate ridges in unheated specimens, as detailed above in the sample description and visible in Fig. 7A–B, are approximately 100–300 nm thick and 100–200 nm high; but in acritarchs heated under anoxic conditions, especially those at 250 days, they are nearly indeterminant and appear more like ghost relics of the initial raised ridges (Fig. 7M–P). This apparent topographic reduction of the reticulations in the anoxic replicates remains unresolved, but the taphonomic consequence is that the structural integrity of the acritarch is preserved at the expense of the intricacy of the reticulate microstructures.

CONCLUSIONS

In an attempt to simulate the processes of carbonization under experimental conditions, we have illustrated the survivorship of organic-walled microfossils with clearly recognizable biological morphologies after controlled heating at 500 °C for relatively long durations. While geological time cannot be replicated in the laboratory, the trends observed in the anoxic replicates indeed indicate that the level of carbonization increases with time: opacity and color showed trends toward more opaque and darker acritarchs, reflectivity became a more prominent feature with increasing time, and graphite-like C–C carbon bonding increased with a corresponding decrease of aldehyde and ketone C=O carbon bonding with increasing heating durations across all anoxic experimental treatment groups. In addition, while the Raman index of D:O intensity may not demonstrate an increase of crystalline ordering during the heating experiment, indicating a lack of true graphitization, RIP did confirm an increase in thermal maturity of the anoxic samples with increasing time—suggesting that time does play an important role in the overall level of carbonization. Each of these separate lines of evidence should be viewed as positive support for observing the process of carbonization throughout the duration of this taphonomic and thermochemical study. In addition, the lack of pervasive destruction of reticulate ridges in anoxic replicates (although certainly not the case in oxic replicates) suggests that the structural decomposition of these ridges may proceed slower than the carbonization processes. However, because acritarchs heated under anoxic conditions do show a reduction of reticulation ridge topography over time, strongly carbonized and graphitized microfossils in the geological record may not preserve the original level of surficial complexity, and intricate microstructures and ornaments could be destroyed more easily than the vesicles themselves during metamorphism.

Despite the limitations noted above, however, organic-walled microfossils may at least retain recognizable morphologies important for their identification as biological entities in the higher-grade metasedimentary rock record. Heating to intermediate to high-grade metamorphic temperatures, whether in anoxic or oxic conditions, is destructive to organic-walled fossils, but the presence of oxygen results in much more aggressive and accelerated degradation than the same temperature and duration of heating in the absence of oxygen. This observation has implications for fossil preservation in Archean and Paleoproterozoic shales deposited prior to the beginning of the Great Oxidation Event at approximately 2450 Ma and also for the preservation and thermochemical transformation in younger metasediments where the nature of fluids and gases are anoxic. The experiments presented here, together with reports of highly metamorphosed and graphitized acritarchs from late Archean-early Paleoproterozoic rocks (Schiffbauer *et al.*, 2007; Zang, 2007), and numerous findings of graphitized or partially graphitized microfossils from younger rocks (Franz *et al.*, 1991; Hanel *et al.*, 1999; Squire *et al.*, 2006; Bernard *et al.*, 2007), verify the survivability of recalcitrant carbonaceous microfossil remains in higher-grade metasediments and provide new preservational clues into a once discounted taphonomic window.

FUTURE DIRECTIONS

As one can appreciate, we could not have possibly performed all applicable analyses on our limited materials. The approaches used here, including a combination of Raman

spectroscopy, XPS, SEM, light microscopy on color, opacity, and reflectivity, and statistical methods, provide a starting point for future work to build upon. It is our hope that these methods will be supplemented by additional analyses. We suggest that an additional suite of analytical approaches such as FTIR and NEXAFS/XANES spectroscopy can be applied to further unravel the thermochemical transformation of carbonaceous material in experimental and metamorphic heating.

ACKNOWLEDGMENTS

We thank T.A. Dexter and P.J. Voice for comments on earlier drafts of the manuscript, C. Farley for technical assistance with Raman spectroscopy and furnace operation, J.W. Huntley for help with sample scoring, C.L. Tyler for statistical assistance, and three anonymous reviewers for constructive comments. This research was funded by the NASA Exobiology and Evolutionary Biology Program, the Virginia Space Grant Consortium, and the Virginia Tech Nanoscale Characterization and Fabrication Laboratory.

REFERENCES

Altermann W, Schopf JW (1995) Microfossils from the Neoarchean Campbell Group, Griqualand West Sequence of the Transvaal Supergroup, and their paleoenvironmental and evolutionary implications. *Precambrian Research* **75**, 65–90.

Awramik SM, Schopf JW, Walter MR (1983) Filamentous fossil bacteria from the Archean of Western Australia. *Precambrian Research* **20**, 357–374.

Batten DJ (1996) Palynofacies and petroleum potential. In *Palynology: Principles and Applications* (eds Jansonius J, Mcgregor DC). American Association of Stratigraphic Palynologists Foundation, Dallas, TX, pp. 1065–1084.

Bény-Bassez C, Rouzaud JN (1985) Characterization of carbonaceous materials by correlated electron optical microscopy and Raman microspectroscopy. *Scanning Electron Microscopy* **1985**, 119–132.

Bernard S, Benzerara K, Beyssac O, Menguy N, Guyot F, Brown GE Jr, Goffé B (2007) Exceptional preservation of fossil plant spores in high-pressure metamorphic rocks. *Earth and Planetary Science Letters* **262**, 257–272.

Beyssac O, Goffé B, Chopin C, Rouzaud JN (2002a) Raman spectra of carbonaceous material in metasediments: a new geothermometer. *Journal of Metamorphic Geology* **20**, 859–871.

Beyssac O, Rouzaud JN, Goffé B, Brunet F, Chopin C (2002b) Graphitization in high-pressure, low-temperature metamorphic gradient: a HRTEM and Raman microspectroscopy study. *Contributions to Mineralogy and Petrology* **143**, 19–31.

Beyssac O, Brunet F, Petitet J, Goffé B, Rouzaud J (2003) Experimental study of the microtextural and structural transformations of carbonaceous materials under pressure and temperature. *European Journal of Mineralogy* **15**, 937–951.

Beyssac O, Bollinger L, Avouac J-P, Goffé B (2004) Thermal metamorphism in the lesser Himalaya of Nepal determined from Raman spectroscopy of carbonaceous material. *Earth and Planetary Science Letters* **225**, 233–241.

Brasier MD, Green OR, Jephcoat AP, Kleppe AK, Kranendonk MJV, Lindsay JF, Steele A, Grassineau NV (2002) Questioning the evidence for Earth's oldest fossils. *Nature* **416**, 76–81.

Buseck PR, Huang BJ (1985) Conversion of carbonaceous material to graphite during metamorphism. *Geochimica et Cosmochimica Acta* **49**, 2003–2016.

Butterfield NJ (1995) Secular distribution of Burgess-Shale-type preservation. *Lethaia* **28**, 1–13.

Butterfield NJ (1996) Fossil preservation in the Burgess Shale: reply. *Lethaia* **29**, 109–112.

Butterfield NJ, Balthasar U, Wilson LA (2007) Fossil diagenesis in the Burgess Shale. *Palaeontology* **50**, 537–543.

Edgington ES, Onghena P (2007) *Randomization Tests*, Chapman & Hall/CRC, Boca Raton, FL.

Ferrari AC, Robertson J (2000) Interpretation of Raman spectra of disordered and amorphous carbon. *Physical Review B* **60**, 14095–14107.

Fischbach DB (1971) The kinetics and mechanism of graphitization. In *Chemistry and Physics of Carbon* (ed. Walker PL Jr). Marcel Dekker, New York, NY, pp. 1–107.

Fitzer E, Mueller K, Schaefer W (1971) The chemistry of the pyrolytic conversion of organic compounds to carbon. In *Chemistry and Physics of Carbon* (ed. Walker PL Jr). Marcel Dekker, New York, NY, pp. 237–385.

Franz G, Mosbrugger V, Menge R (1991) Carbo-Permian pteridophyll leaf fragments from an amphibolite facies basement, Tauern Window, Austria. *Terra Nova* **3**, 137–141.

Grew ES (1974) Carbonaceous material in some metamorphic rocks of New England and other areas. *Journal of Geology* **82**, 50–73.

Gutjahr CCM (1966) Carbonization measurements of pollen-grains and spores and their application. *Leidse Geologische Mededelingen* **38**, 1–29.

Hammer Ø, Harper DAT, Ryan PD (2001) PAST: Paleontological statistics software package for education and data analysis. *Palaeontologia Electronica* **4**, 1–9.

Hanel M, Montenari M, Kalt A (1999) Determining sedimentation ages of high-grade metamorphic gneisses by their palynological record: a case study in the northern Schwarzwald (Variscan Belt, Germany). *International Journal of Earth Sciences* **88**, 49–59.

Hofmann HJ, Schopf JW (1983) Early Proterozoic microfossils. In *Earth's Earliest Biosphere, Its Origin and Evolution* (ed. Schopf JW). Princeton University Press, Princeton, NJ, pp. 321–360.

Horita J (2005) Some perspectives on isotope biosignatures for early life. *Chemical Geology* **218**, 171–186.

Hunt JM (1996) *Petroleum Geochemistry and Geology*, W.H. Freeman, New York, NY.

Javaux EJ, Knoll AH, Walter MR (2001) Morphological and ecological complexity in early eukaryotic ecosystems. *Nature* **412**, 66–69.

Javaux EJ, Knoll AH, Walter MR (2004) TEM evidence for eukaryotic diversity in mid-Proterozoic oceans. *Geobiology* **2**, 121–132.

Jehlička J, Bény C (1992) Application of Raman microspectrometry in the study of structural changes in Precambrian kerogens during regional metamorphism. *Organic Geochemistry* **18**, 211–213.

Jehlička J, Bény C (1999) First and second order Raman spectra of natural highly carbonified organic compounds from metamorphic rocks. *Journal of Molecular Structure* **480–481**, 541–545.

Jehlička J, Bény C, Rouzaud JN (1997) Raman microspectrometry of accumulated non-graphitized bitumens. *Journal of Raman Spectoscopy* **28**, 717–724.

Jehlička J, Urban A, Pokorny J (2003) Raman spectroscopy of carbon and solid bitumens in sedimentary and metamorphic rocks. *Spectrochimica Acta A* **59**, 2341–2352.

Kidder DL, Awramik SM (1990) Acritarchs in lower greenschist facies argillite of the middle Proterozoic Libby Formation, Upper Belt Supergroup, Montana. *Palaios* **5**, 124–133.

Knoll AH (1992) Microfossils in metasedimentary cherts of the Scotia Group, Prins Karls Forland, western Svalbard. *Palaeontology* **35**, 751–774.

Knoll AH, Barghoorn ES (1977) Archean microfossils showing cell-division from Swaziland System of South Africa. *Science* **198**, 396–398.

Knoll AH, Strother PK, Rossi S (1988) Distribution and diagenesis of microfossils from the Lower Proterozoic Duck Creek Dolomite, Western Australia. *Precambrian research* **38**, 257–279.

Kowalewski M, Novack-Gottshall P (2010) Resampling methods in paleontology. In *Quantitative Methods in Paleobiology* (eds Alroy J, Hunt G). Paleontological Society Special Papers, New Haven, CT, pp. 19–54.

Kowalewski M, Goodfriend GA, Flessa KW (1998) High-resolution estimates of temporal mixing within shell beds: the evils and virtues of time-averaging. *Paleobiology* **24**, 287–304.

Landis CA (1971) Graphitization of dispersed carbonaceous material in metamorphic rocks. *Contributions to Mineralogy and Petrology* **30**, 34–45.

Large DJ, Christy AG, Fallick AE (1994) Poorly crystalline carbonaceous matter in high grade metasediments: implications for graphitization and metamorphic fluid compositions. *Contributions to Mineralogy and Petrology* **116**, 108–116.

Marshall CP, Mar GL, Nicoll RS, Wilson MA (2001) Organic geochemistry of artificially matured conodonts. *Organic Geochemistry* **32**, 1055–1071.

Marshall CP, Javaux EJ, Knoll AH, Walter MR (2005) Combined micro-Fourier transform infrared (FTIR) spectroscopy and micro-Raman spectroscopy of Proterozoic acritarchs: a new approach to Palaeobiology. *Precambrian Research* **138**, 208–224.

Marshall CP, Edwards HGM, Jehlicka J (2010) Understanding the application of Raman spectroscopy to the detection of traces of life. *Astrobiology* **10**, 229–243.

Mendelson CV, Schopf JW (1992) Proterozoic and selected Early Cambrian microfossils and microfossillike objects. In *The Proterozoic Biosphere: A Multidisciplinary Study* (eds Schopf JW, Klein C). Cambridge University Press, New York, NY, pp. 865–951.

Mojzsis SJ, Arrhenius G, Mckeegan KD, Harrison TM, Nutman AP, Friend CRL (1996) Evidence for life on Earth by 3800 million years ago. *Nature* **384**, 55–59.

Molyneux SG (1998) An upper Dalradian microfossil reassessed. *Journal of the Geological Society, London* **155**, 741–743.

Nagovitsin K (2009) Tappania-bearing association of the Siberian platform: biodiversity, stratigraphic position and geochronological constraints. *Precambrian Research* **173**, 137–145.

Negri F, Castiglioni C, Tommasini M, Zerbi G (2002) A computational study of the Raman spectra of large polycyclic aromatic hydrocarbons: toward molecularly defined subunits of graphite. *The Journal of Physical Chemistry A* **106**, 3306–3317.

Nestler K, Dietrich D, Witke K, Röβler R, Marx G (2003) Thermogravimetric and Raman spectroscopic investigations on different coals in comparison to dispersed anthracite found in permineralized tree fern *Psaronius* sp. *Journal of Molecular Structure* **661–662**, 357–362.

Ohmoto H, Kakegawa T, Lowe DR (1993) 3.4-billion-year-old biogenic pyrites from Barberton, South Africa: sulfur isotope evidence. *Science* **262**, 555–557.

Orr PJ, Briggs DEG, Kearns SL (1998) Cambrian Burgess Shale animals replicated in clay minerals. *Science* **281**, 1173–1175.

Papineau D, Mojzsis SJ (2006) Mass-independent fractionation of sulfur isotopes in sulfides from the pre-3770 Ma Isua Supracrustal Belt, West Greenland. *Geobiology* **4**, 227–238.

Pasteris JD, Wopenka B (1991) Raman spectra of graphite as indicators of degree of metamorphism. *Canadian Mineralogist* **29**, 1–9.

Pasteris JD, Wopenka B (2002) Laser–Raman spectroscopy (Communication arising): images of the Earth's earliest fossils? *Nature* **420**, 476–477.

Pasteris JD, Wopenka B (2003) Necessary, but not sufficient: Raman identification of disordered carbon as a signature of ancient life. *Astrobiology* **3**, 727–738.

Peters KE, Ishiwatari R, Kaplan IR (1977) Color of kerogen as index of organic maturity. *American Association of Petroleum Geologists Bulletin* **61**, 504–510.

Powell W (2003) Greenschist-Facies Metamorphism of the Burgess Shale and its implications for models of fossil formation and preservation. *Canadian Journal of Earth Sciences* **40**, 13–25.

Prasad B, Asher R (2001) Acritarch biostratigraphy and lithostratigraphic classification of Proterozoic and lower Paleozoic sediments (pre-unconformity sequence) of Ganga Basin, India. *Paleontographica Indica* **5**, 1–151.

Prasad B, Uniyal SN, Asher R (2005) Organic-walled microfossils from the Proterozoic Vindhyan Supergroup of Son Valley, Madhya Pradesh, India. *Palaeobotanist* **54**, 13–60.

Schiffbauer JD, Xiao S (2009) Novel application of focused ion beam electron microscopy (FIB-EM) in preparation and analysis of microfossils ultrastructures: a new view of complexity in early eukaryotic organisms. *Palaios* **24**, 616–626.

Schiffbauer JD, Yin L, Bodnar RJ, Kaufman AJ, Meng F, Hu J, Shen B, Yuan X, Bao H, Xiao S (2007) Ultrastructural and geochemical characterization of Archean-Paleoproterozoic graphite particles: implications for recognizing traces of life in highly metamorphosed rocks. *Astrobiology* **7**, 684–704.

Schopf JW (2006) Fossil evidence of Archaean life. *Philosophical Transactions of the Royal Society B* **361**, 869–885.

Schopf JW, Walter MR (1983) Archean microfossils: new evidence of ancient microbes. In *Earth's Earliest Biosphere: Its Origin and Evolution* (ed. Schopf JW). Princeton University Press, Princeton, NJ, pp. 214–239.

Schopf JW, Kudryavtsev AB, Agresti DG, Wdowiak TJ, Czaja AD (2002) Laser–Raman spectroscopy (Communication arising): images of the Earth's earliest fossils? Reply *Nature* **420**, 477.

Schopf JW, Kudryavtsev AB, Agresti DG, Czaja AD, Wdowiak TJ (2005) Raman imagery: a new approach to assess the geochemical maturity and biogenicity of permineralized Precambrian fossils. *Astrobiology* **5**, 333–371.

Schweitzer MH, Avci R, Collier T, Goodwin MB (2008) Microscopic, chemical and molecular methods for examining fossil preservation. *Comptes Rendus Palevol* **7**, 159–184.

Senftle JT, Landis CR (1991) Vitrinite reflectance as a tool to assess thermal maturity. In *Source and Migration Processes and Evaluation Techniques; Treatise of Petroleum Geology* (ed. Merrill RK). American Association of Petroleum Geologists, Tulsa, OK, pp. 119–125.

Spotl C, Houseknecht DW, Jaques RC (1998) Kerogen maturation and incipient graphitization of hydrocarbon source rocks in the Arkoma Basin, Oklahoma and Arkansas: a combined petrographic and Raman study. *Organic Geochemistry* **28**, 535–542.

Squire RJ, Stewart IR, Zang WL (2006) Acritarchs in polydeformed and highly altered Cambrian rocks in western Victoria. *Australian Journal of Earth Sciences* **53**, 697–705.

Staplin FL (1969) Sedimentary organic matter, organic metamorphism, and oil and gas occurrence. *Bulletin of Canadian Petroleum Geology* **17**, 47–66.

Stipp SL, Hochella MF (1991) Structure and bonding environments at the calcite surface as observed with X-ray photoelectron spectros-

copy (XPS) and low energy electron diffraction (LEED). *Geochemica et Cosmochimica Acta* **55**, 1723–1736.
Summons RE, Jahnke LL, Hope JM, Logan GA (1999) 2-Methylhopanoids as biomarkers for cyanobacterial oxygenic photosynthesis. *Nature* **400**, 554–557.
Toporski JKW, Steele A, Westall F, Avci R, Martill DM, McKay DS (2002) Morphologic and spectral investigation of exceptionally well-preserved bacterial biofilms from the Oligocene Enspel Formation, Germany. *Geochimica et Cosmochimica Acta* **66**, 1773–1791.
Tuinstra F, Koenig JL (1970) Raman spectrum of graphite. *The Journal of Chemical Physics* **53**, 1126–1130.
Van Zuilen MA, Lepland A, Arrhenius G (2002) Reassessing the evidence for the earliest traces of life. *Nature* **418**, 627–630.
Vandenbroucke M (2003) Kerogen: from types to models of chemical structure. *Oil & Gas Science and Technology/ Revue de l'Institut Francais du Petrole* **58**, 243–269.
Vandenbroucke M, Largeau C (2007) Kerogen origin, evolution and structure. *Organic Geochemistry* **38**, 719–833.
Vickerman JC, Gilmore IS (2009) *Surface Analysis: The Principal Techniques*, John Wiley and Sons, Chichester, UK.
Vidal G (1988) A palynological preparation method. *Palynology* **12**, 215–220.
Wada H, Tomita T, Matsuura K, Iuchi K, Ito M, Morikiyo T (1994) Graphitization of carbonaceous matter during metamorphism with references to carbonate and pelitic rocks of contact and regional metamorphism, Japan. *Contributions to Mineralogy and Petrology* **118**, 217–228.
Wagner CD, Riggs WM, Davis LE, Moulder JF, Muilenberg GE (1979) *Handbook of X-ray Photoelectron Spectroscopy*, Perkin-Elmer Corporation, Eden Prairie, MN.
Walsh MM, Lowe DR (1985) Filamentous microfossils from the 3,500-myr-old Onverwacht Group, Barberton Mountain Land, South Africa. *Nature* **314**, 530–532.
Wojdyr M (2010) Fityk: a general-purpose peak fitting program. *Journal for Applied Crystallography* **43**, 1126–1128.
Wopenka B, Pasteris JD (1993) Structural characterization of kerogens to granulite-facies graphite: applicability of Raman microprobe spectroscopy. *American Mineralogist* **78**, 533–557.
Xiao S, Knoll AH, Kaufman AJ, Yin L, Zhang Y (1997) Neoproterozoic fossils in Mesoproterozoic rocks? Chemostratigraphic resolution of a biostratigraphic conundrum from the North China Platform *Precambrian Research* **84**, 197–220.
Yin L (1997) Acanthomorphic acritarchs from Meso-Neoproterozoic shales of the Ruyang Group, Shanxi, China. *Review of Palaeobotany and Palynology* **98**, 15–25.
Yin L, Xunlai Y, Fanwei M, Jie H (2005) Protists of the Upper Mesoproterozoic Ruyang Group in Shanxi Province, China. *Precambrian Research* **141**, 49–66.
Yui T-F, Huang E, Xu J (1996) Raman spectrum of carbonaceous material: a possible metamorphic grade indicator for low-grade metamorphic rocks. *Journal of Metamorphic Geology* **14**, 115–124.
Zang W-L (2007) Deposition and deformation of late Archean sediments and preservation of microfossils in the Harris Greenstone Domain, Gawler Craton, South Australia. *Precambrian Research* **156**, 107–124.

APPENDIX A

Full data table reporting measured optical and Raman-based thermal alteration indices. Opacity index (*Oi*) recorded as scored (0–3); values in parentheses indicate initial discrepancy in scoring, corresponding resolved value outside parentheses. Reflectivity index (*Ri*) values represent recalculated values from initial 0–2 scale. Peak intensity and area ratios [D:O; D/(D + O) × 100] and Raman Index of Preservation (RIP) were calculated from baseline corrected Raman spectra. Raw RIP values (not shown) calibrated following Schopf *et al.* (2005).

Sample number	Heating duration (days)	Preparation	*Oi*	*Ri*	D:O	D/(D + O) × 100	Calibrated RIP
1	0	Control	1	0	0.63	59.07	7.38
2	0	Control	1	0	0.67	58.87	7.98
3	0	Control	2	0	0.69	60.42	8.86
4	0	Control	1	0	0.68	59.72	8.24
5	0	Control	1	1	0.67	60.26	8.57
6	0	Control	1	1	0.69	60.26	8.48
7	0	Control	2	0	0.72	60.57	8.39
8	0	Control	3	0	0.74	59.54	8.35
9	0	Control	1	0	0.67	60.24	8.55
10	0	Control	1	1	0.65	59.96	8.47
11	0	Control	1	0	0.73	59.67	7.80
12	0	Control	3	0	0.76	60.06	8.30
13	0	Control	2 (3)	0	0.67	58.10	7.82
14	0	Control	1	0	0.67	59.59	8.33
15	0	Control	1	0	0.68	60.66	9.00
16	0	Control	1	0	0.70	60.01	8.27
17	0	Control	2	0	0.68	59.77	8.40
18	0	Control	2	0	0.71	58.93	7.98
19	0	Control	1	0	0.70	60.28	8.57
20	0	Control	0	0	0.65	57.97	8.40
21	0	Control	1	0	0.67	59.96	8.36
22	0	Control	1	0	0.66	60.03	8.46

APPENDIX A: (*Continued*)

Sample number	Heating duration (days)	Preparation	*Oi*	*Ri*	D:O	D/(D + O) × 100	Calibrated RIP
23	0	Control	3	1	0.73	59.62	8.04
24	0	Control	1	0	0.65	59.35	8.01
25	0	Control	1	0	0.68	59.90	8.35
26	0	Control	1	0	0.68	60.32	8.41
27	0	Control	1	0	0.67	60.26	8.79
28	0	Control	2	0	0.65	58.84	7.77
29	0	Control	1	0	0.67	59.90	8.34
30	0	Control	1	0	0.65	59.50	8.20
31	0	Control	1	0	0.74	60.20	8.10
32	0	Control	1	0	0.66	60.01	8.43
33	0	Control	1	0	0.67	59.99	8.62
34	0	Control	1	0	0.67	58.17	8.90
35	0	Control	2	1	0.62	59.63	8.08
36	0	Control	1	1	0.67	59.83	8.03
37	0	Control	1	0	0.70	59.61	8.00
38	0	Control	2	0	0.67	59.91	8.25
39	0	Control	2	0	0.67	60.06	8.46
40	0	Control	1	0	0.68	59.86	8.41
41	0	Control	1	0	0.64	59.82	8.34
42	0	Control	1	0	0.67	60.31	8.63
43	0	Control	2	0	0.67	59.49	8.07
44	0	Control	1	0	0.60	59.87	7.98
45	0	Control	0	0	0.68	59.04	7.95
46	0	Control	1	0	0.64	59.54	8.36
47	0	Control	1	0	0.70	60.19	8.14
48	0	Control	1	0	0.66	58.94	7.96
49	0	Control	2	0	0.65	59.91	8.43
50	0	Control	1	0	0.66	59.82	8.44
		Mean	1.30	0.12	0.68	59.72	8.29
51	1	Oxic	1	0	0.68	59.91	8.31
52	1	Oxic	2	1	0.64	59.69	8.29
53	1	Oxic	2	0	0.67	60.38	8.67
54	1	Oxic	1	0	0.69	60.72	8.86
55	1	Oxic	0	0	0.68	59.77	8.41
56	1	Oxic	1	1	0.66	60.49	8.76
57	1	Oxic	3	1	0.67	60.55	8.92
58	1	Oxic	2 (1)	0	0.66	59.84	8.12
59	1	Oxic	3	1	0.74	60.24	8.25
60	1	Oxic	1	0	0.65	60.15	8.54
61	1	Oxic	1 (2)	0	0.61	60.05	8.45
62	1	Oxic	1	0	0.63	60.49	8.61
63	1	Oxic	1	1	0.62	59.89	8.13
64	1	Oxic	3	1	0.69	60.13	8.40
65	1	Oxic	2	0	0.69	60.35	8.58
66	1	Oxic	3	0	0.67	60.69	8.47
67	1	Oxic	3	0	0.69	60.28	8.43
68	1	Oxic	2	1	0.68	60.44	8.75
69	1	Oxic	1	0	0.67	59.74	8.28
70	1	Oxic	2	0	0.69	60.13	8.32
71	1	Oxic	2	1	0.70	60.65	8.84
72	1	Oxic	2	0	0.66	60.24	8.74
73	1	Oxic	2	0	0.63	60.00	8.21
74	1	Oxic	2	0	0.66	60.40	8.54
		Mean	1.79	0.33	0.67	60.22	8.49
75	3	Oxic	1	0	0.79	61.27	8.04
76	3	Oxic	1	0	0.70	60.90	8.64
77	3	Oxic	1	0	0.69	59.95	8.41

APPENDIX A: (*Continued*)

Sample number	Heating duration (days)	Preparation	*Oi*	*Ri*	D:O	D/(D + O) × 100	Calibrated RIP
78	3	Oxic	1	0	0.68	60.08	8.67
79	3	Oxic	1	1	0.75	59.62	7.61
80	3	Oxic	0	0	0.71	59.27	7.18
81	3	Oxic	2	1	0.71	60.64	8.63
82	3	Oxic	1	0	0.71	59.60	7.84
83	3	Oxic	2	0	0.74	58.41	7.12
84	3	Oxic	1	0	0.72	61.36	7.92
85	3	Oxic	1	1	0.67	58.99	6.64
86	3	Oxic	1	0	0.74	59.91	7.44
87	3	Oxic	0	0	0.75	59.90	8.00
88	3	Oxic	0	0	0.79	60.35	6.22
89	3	Oxic	3 (2)	1	0.65	58.96	7.49
90	3	Oxic	1	0	0.71	59.62	8.11
91	3	Oxic	3	1	0.67	58.85	8.29
92	3	Oxic	2	1	0.65	58.05	7.47
93	3	Oxic	1	1	0.69	59.22	7.52
94	3	Oxic	0	0	0.66	59.65	7.62
95	3	Oxic	0	0	0.66	59.77	7.86
96	3	Oxic	0	0	0.71	59.92	8.27
97	3	Oxic	0	0	0.66	59.12	7.84
98	3	Oxic	0	0	0.67	59.35	8.10
99	3	Oxic	1	0	0.69	58.90	7.19
		Mean	0.96	0.28	0.70	59.67	7.77
100	5	Oxic	0	0	0.72	59.48	7.45
101	5	Oxic	0	0	0.68	59.37	8.35
102	5	Oxic	0	1	0.69	59.63	7.69
103	5	Oxic	1	0	0.71	58.85	7.03
104	5	Oxic	2	0	0.65	59.40	8.27
105	5	Oxic	2	1	0.69	59.50	7.74
106	5	Oxic	0	1	0.64	59.07	7.80
107	5	Oxic	0	0	0.68	59.56	8.14
108	5	Oxic	0	1	0.74	58.93	7.40
109	5	Oxic	1	0	0.77	60.37	7.95
110	5	Oxic	0	0	0.73	59.35	8.34
111	5	Oxic	1	0	0.71	59.85	8.18
112	5	Oxic	1	0	0.71	60.67	8.55
113	5	Oxic	1	0	0.75	58.73	6.63
114	5	Oxic	2	0	0.71	60.70	8.80
115	5	Oxic	0	0	0.67	59.78	8.46
116	5	Oxic	1	0	0.65	59.29	8.54
117	5	Oxic	2	1	0.72	60.22	7.77
118	5	Oxic	0	0	0.71	59.91	8.31
		Mean	0.74	0.26	0.70	59.61	7.97
119	5	Anoxic	2	1	0.67	59.71	7.96
120	5	Anoxic	1	0	0.58	59.06	7.91
121	5	Anoxic	2	0	0.60	59.71	8.66
122	5	Anoxic	2	0	0.56	59.02	8.06
123	5	Anoxic	1	0	0.58	59.26	8.48
124	5	Anoxic	1	0	0.60	59.18	8.32
125	5	Anoxic	2	1	0.62	59.88	7.99
126	5	Anoxic	3	1	0.59	59.61	7.97
127	5	Anoxic	1	0	0.58	59.34	8.42
128	5	Anoxic	2	1	0.57	58.67	8.07
129	5	Anoxic	1	1	0.55	59.08	8.01
130	5	Anoxic	2	0	0.58	59.34	8.23
131	5	Anoxic	1	1	0.58	58.68	7.87
132	5	Anoxic	1	0	0.62	59.99	8.16
133	5	Anoxic	1	0	0.58	59.65	8.38

APPENDIX A: (*Continued*)

Sample number	Heating duration (days)	Preparation	*Oi*	*Ri*	D:O	D/(D + O) × 100	Calibrated RIP
134	5	Anoxic	1	1	0.58	59.36	8.10
135	5	Anoxic	1	0	0.60	59.47	8.03
136	5	Anoxic	1	0	0.56	59.35	8.02
137	5	Anoxic	1	1	0.60	58.25	7.58
138	5	Anoxic	1	0	0.57	58.55	8.08
		Mean	1.40	0.40	0.59	59.26	8.11
139	125	Anoxic	2	0	0.72	59.83	7.46
140	125	Anoxic	2	1	0.74	60.72	8.39
141	125	Anoxic	1	0	0.73	60.33	8.15
142	125	Anoxic	3	0	0.74	60.19	8.05
143	125	Anoxic	3	1	0.79	60.24	7.67
144	125	Anoxic	3	1	0.76	60.70	8.25
145	125	Anoxic	2	0	0.77	60.65	8.13
146	125	Anoxic	1	1	0.77	60.14	7.95
147	125	Anoxic	1	0	0.78	60.79	8.35
148	125	Anoxic	1	0	0.75	59.63	7.66
149	125	Anoxic	1	0	0.79	60.68	8.84
150	125	Anoxic	2	1	0.77	59.47	7.62
151	125	Anoxic	2	1	0.81	60.13	7.85
152	125	Anoxic	1	1	0.73	59.94	7.80
153	125	Anoxic	3 (2)	0	0.74	60.04	8.58
154	125	Anoxic	2	0	0.74	59.75	7.68
155	125	Anoxic	2	1	0.75	60.45	8.16
156	125	Anoxic	1 (2)	1	0.73	60.48	8.16
157	125	Anoxic	1	1	0.73	60.47	8.10
158	125	Anoxic	1	1	0.79	60.51	8.02
		Mean	1.75	0.55	0.76	60.26	8.04
159	250	Anoxic	3	1	0.67	60.04	8.11
160	250	Anoxic	3	1	0.69	59.89	7.69
161	250	Anoxic	2	1	0.71	59.86	8.01
162	250	Anoxic	2	1	0.64	60.42	9.09
163	250	Anoxic	2	1	0.67	59.76	8.11
164	250	Anoxic	1	1	0.69	60.27	8.13
165	250	Anoxic	3	1	0.68	59.73	8.23
166	250	Anoxic	1	1	0.68	60.01	8.03
167	250	Anoxic	3	0	0.68	59.47	7.60
168	250	Anoxic	1	0	0.67	60.51	8.67
169	250	Anoxic	2	1	0.67	59.88	7.80
170	250	Anoxic	3	0	0.65	59.42	8.07
171	250	Anoxic	2	0	0.69	59.10	7.92
172	250	Anoxic	2	0	0.65	59.42	7.82
173	250	Anoxic	2	1	0.72	60.37	7.93
174	250	Anoxic	2	1	0.91	60.53	7.52
175	250	Anoxic	2	0	0.68	59.81	8.08
176	250	Anoxic	2	1	0.75	60.07	7.93
177	250	Anoxic	2	0	0.69	60.33	7.82
178	250	Anoxic	1	1	0.75	60.09	8.10
179	250	Anoxic	3	0	0.73	59.59	7.64
		Mean	2.10	0.62	0.70	59.93	8.01